



Arena, G., Groh, R., Pirrera, A., Turner, T., Scholten, W., & Hartl, D. (2021). Design of Shape-Adaptive Deployable Slat-Cove Filler for Airframe Noise Reduction. *Journal of Aircraft*, 58(5), 1034-1050. <https://doi.org/10.2514/1.C036070>

Publisher's PDF, also known as Version of record

License (if available):
CC BY

Link to published version (if available):
[10.2514/1.C036070](https://doi.org/10.2514/1.C036070)

[Link to publication record on the Bristol Research Portal](#)
PDF-document

This is the final published version of the article (version of record). It first appeared online via American Institute of Aeronautics and Astronautics at <https://doi.org/10.2514/1.C036070> . Please refer to any applicable terms of use of the publisher.

University of Bristol – Bristol Research Portal

General rights

This document is made available in accordance with publisher policies. Please cite only the published version using the reference above. Full terms of use are available: <http://www.bristol.ac.uk/red/research-policy/pure/user-guides/brp-terms/>



Design of Shape-Adaptive Deployable Slat-Cove Filler for Airframe Noise Reduction

Gaetano Arena,^{*} Rainer M. J. Groh,[†] and Alberto Pirrera[‡]
University of Bristol, Bristol, England BS8 1TR, United Kingdom
 Travis Turner[§]

NASA Langley Research Center, Hampton, Virginia 23681
 and

William Scholten[¶] and Darren Hartl^{**}
Texas A&M University, College Station, Texas 77843

<https://doi.org/10.2514/1.C036070>

Mechanical instabilities and elastic nonlinearities are emerging means for designing deployable and shape adaptive structures. Dynamic snap-through buckling is investigated here as a means to tailor the deployment and retraction of a slat-cove filler (SCF), a morphing component used to reduce airframe noise. Upon deployment, leading-edge slats create a cove between themselves and the main wing, producing unsteady flow features that are a significant source of airframe noise. A SCF is designed here to autonomously snap out as the slat deploys, providing a smoother aerodynamic profile that reduces flow unsteadiness. The nonlinear structural behavior of the SCF is studied, and then tailored, to achieve a desirable snapping response. Three SCF configurations are considered: 1) a constant thickness (monolithic) superelastic shape-memory alloy (SMA) SCF, 2) a variable-thickness SMA SCF, and 3) a set of stiffness-tailored fiberglass composite SCFs. Results indicate that, although monolithic SMA SCFs provide a simple solution, thickness variations in both the SMA and stiffness-tailored composite SCF designs allow a decrease of the energy required for self-deployment and a reduction of the severity of the impact between the SCF and the slat during stowage. The enhanced nonlinear behavior from stiffness tailoring reduces peak material strains in comparison to previous SMA SCF designs that leveraged material superelasticity for shape adaptation. The stiffness tailoring is readily achieved through the use of layered composites, facilitating considerable weight savings compared to the dense SMA designs. The aeroelastic response of different SCFs is calculated using fluid/structure interaction analyses, and it is shown that both SMA and composite SCF designs can deploy and retract in full flow conditions.

Nomenclature

C^A, C^M	= stress-temperature ratios for Austenite and Martensite phases, Pa/K
E	= elastic modulus, Pa
E^A, E^M	= elastic modulus for Austenite and Martensite phases, Pa
F	= transverse load, N
H	= transformation strain
I_F	= Tsai–Wu failure index
KE	= area specific kinetic energy, J/m ²
S	= shear strength, Pa
SE	= strain energy, J
u	= compressive axial displacement, m
v	= velocity, m/s
X	= longitudinal direction along fibers
Y	= transverse direction across fibers
δ	= central deflection, m

ϵ_x	= strain in x direction, %
ρ	= density, kg/m ³
σ_x	= stress in x direction, Pa
σ_{xz}	= transverse shear stress, Pa
σ^{As}, σ^{Af}	= critical stresses for start and end of transformation to Austenite, Pa
σ^{Ms}, σ^{Mf}	= critical stresses for start and end of transformation to Martensite, Pa
ν_A, ν_M	= Poisson’s ratio for Austenite and Martensite phases
ν_{12}	= Poisson’s ratio for fiberglass

I. Introduction

SHape-changing structures can adapt in response to varying operating conditions, thereby optimizing performance under more than one design point [1–4]. Specifically, morphing behavior can be induced by tailoring properties of the constituent materials [5–7] and/or by designing stress fields into structural components [8,9]. The latter case can cause mechanical instabilities and geometrically nonlinear elastic responses. The use of mechanical instabilities to enable morphing capabilities is particularly useful when a system requires large deformations or benefits from multiple configurations [10–13]. Often, multistable snap-through behavior is achieved by toggling between different postbuckled states [10,14–16].

In this Paper, we apply the adaptation-by-instability approach to investigate and tailor the nonlinear structural response of a slat-cove filler (SCF), a novel noise-reduction device to be employed on transport aircraft. Originally proposed by Gleine et al. [17], the SCF is a morphing component used to fill the cove between the deployed leading-edge slat and the main wing in transport class aircraft (see Fig. 1). When high-lift devices are deployed during the low-speed maneuvers of approach and landing at low altitudes, geometric discontinuities associated with the leading-edge slat cove induce unsteady circulation and other flow features that lead to elevated levels of airframe noise (see Fig. 1a) [18,19], a growing concern in the aerospace community. The function of the SCF is to alter the outer

Received 2 July 2020; revision received 18 December 2020; accepted for publication 20 December 2020; published online Open Access 12 April 2021. Copyright © 2021 by the authors. Published by the American Institute of Aeronautics and Astronautics, Inc., with permission. All requests for copying and permission to reprint should be submitted to CCC at www.copyright.com; employ the eISSN 1533-3868 to initiate your request. See also AIAA Rights and Permissions www.aiaa.org/randp.

^{*}EPSRC Doctoral Prize Fellow, Bristol Composites Institute (ACCIS); currently Materials Applications Engineer, Rolls–Royce; gaetano.arena@rolls-royce.com.

[†]Royal Academy of Engineering Research Fellow, Bristol Composites Institute (ACCIS); rainer.groh@bristol.ac.uk.

[‡]Associate Professor, Nonlinear Structural Mechanics, Bristol Composites Institute (ACCIS); alberto.pirrera@bristol.ac.uk.

[§]Research Engineer, Structural Acoustics Branch, Associate Fellow AIAA.

[¶]Graduate Research Assistant, Department of Aerospace Engineering; currently Project Engineer, ATA Engineering; william.scholten@ata-e.com.

^{**}Assistant Professor, Department of Aerospace Engineering; darren.hartl@tamu.edu.

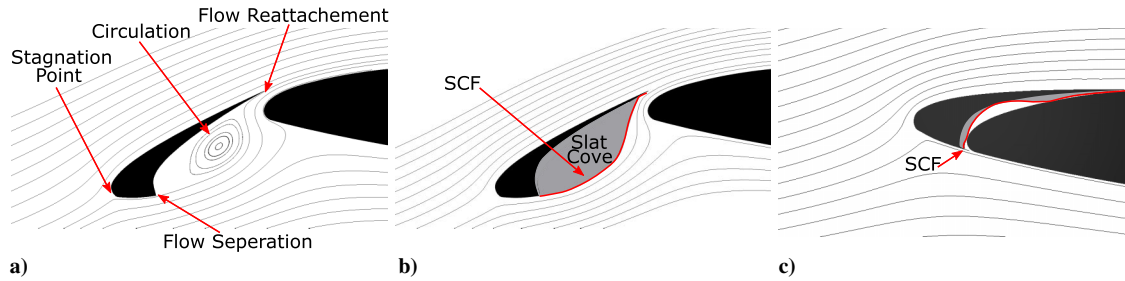


Fig. 1 Operation of the SCF: a) flow separation and consequent air circulation caused by the discontinuity of the slat geometry and SCF in its b) deployed and c) retracted configurations.

mold line of the deployed leading-edge slat such that the airflow is modified into an acoustically advantageous state, without affecting the beneficial lift-generating qualities of the leading-edge slat (see Fig. 1b) [17]. This concept has been shown to be effective at noise reduction both experimentally [20–24] and computationally [25,26]. Alternative noise mitigation attempts include extended blade seals [27], brushes [28,29], mass injection [30], and the slat-gap filler^{††} [31,32].

A thin shell SCF concept is considered in this Paper as it has been shown to be structurally effective at maintaining its shape under aerodynamic flow and deforming into a stowed position between the slat and main wing (see Fig. 1c) as the high-lift devices are retracted [33,34]. Work on the thin shell SCF concept began with the development of physical benchtop models [34] that incorporated shape-memory alloys (SMAs), a type of active material that undergoes a solid-phase transformation when subjected to sufficient thermal or mechanical load, allowing for large recoverable deformations [35]. Following the benchtop models, structural finite element models of the SMA-based SCF design were developed, and optimization was performed with a focus of reducing actuation force required to stow the SCF [33]. Work then shifted toward the development of both computational fluid dynamics (CFD) and fluid/structure interaction (FSI) models to assess the SCF behavior in relevant flowfield environments [36–38]. Concurrently with the computational CFD/FSI model development, a scaled physical model with deployable slat/flaps and a SMA SCF was built. Wind tunnel testing at various wing configurations/flow conditions and structural experiments with digital image correlation were performed to begin validation of the computational models [37–39]. Further work has also focused on computational modeling of fully mechanized benchtop models [40]. A novelty of this Paper is that, for the first time, the effects of FSI analysis on the SCF design are evaluated and the importance of coupled analysis in the design is highlighted.

To avoid the addition of heavy and bulky actuators, the retraction and deployment of the SCF should ideally be induced in a passive manner. One means of achieving passive adaptation is by exploiting geometric and/or material nonlinearities. The stowed configuration of Fig. 1c can be designed to be statically unstable when no load is acting on the SCF. In such designs, as the leading-edge slat deploys, the SCF may autonomously snap out into its deployed shape, thereby filling the cove. The deployment of the SCF can therefore be entirely governed by nonlinear mechanics, in other words, a geometrically or constitutively nonlinear restoring force. In this Paper, we consider constitutive nonlinearity in the case of SMA SCFs and geometric nonlinearity in all designs, as it can be exploited regardless of the material system used.

Because of the nonlinearity of the problem, developing a robust design methodology is a challenge. Here, we propose and test a design methodology that uses finite element structural analysis and CFD simulations. While previous work has focused predominantly on using SMA materials for the SCF [6,33,36–38], a novelty of the present Paper is the consideration of lightweight composite materials for the first time. In particular, the influence of material selection is investigated by comparing three SCF configurational classes:

1) a uniformly thick (monolithic) SMA SCF, 2) a variable-thickness SMA SCF, and 3) a fiberglass composite SCF having a carefully designed layout. SMA materials are a natural choice for deployable SCFs due to the intrinsic superelastic properties [38]. However, a similar reversible, elastic behavior that permits extreme deformations can also be achieved geometrically, rather than constitutively, by exploiting elastic instabilities, in other words, snap-through buckling [10,14]. In this case, laminated composites are particularly attractive due to their excellent mass-specific properties and because, by varying the stacking sequence, the elastic properties and failure limits of a laminate can be readily modified. Consequently, a higher control on the tailoring of the nonlinear structural response of the SCF retraction/deployment process is permitted.

The remainder of the Paper is organized as follows. Section II provides a short theoretical background to elastic instability pertaining to shape adaptation. Section III describes the structural and aerodynamic analysis tools used and outlines the design constraints during the tailoring process. Section IV discusses the tailoring process and presents dynamic structural and fluid/structure interaction analyses of different SCF designs. Conclusions and suggestions for future work are discussed in Sec. V.

II. Elastic Instabilities and Shape Adaptation

Figure 2 shows the retraction/deployment process of a generic SCF as driven by contact with the main wing. As the SCF is displaced from its fully deployed shape due to contact with the main wing (Figs. 2b and 2c), it deflects toward the slat. Since the trailing portion of the SCF is constrained to slide in the small space between the main wing and slat, its leading portion temporarily becomes unstable and separates from the wing (Fig. 2d) until contact with the slat-cove wall restabilizes it. Finally, the wing deforms the SCF sufficiently to cause snap-through into the inverted and retracted (stowed) configuration, as shown in Figs. 2e and 2f.

During deployment, the point of contact between the SCF and main wing moves progressively toward the leading end of the SCF until the SCF becomes unstable and is free to snap back into its deployed shape (Figs. 2h–2l). The retraction and deployment of the SCF is therefore governed by the constraint applied by the contact between the wing and the SCF. In summary, 1) during retraction, the main wing pushes the SCF into its stowed configuration aided by the nonlinear mechanics of the SCF that progressively reduces its rigidity, while 2) during deployment, the SCF slides along the main wing until the restraint that the wing provides is no longer sufficient to prevent the SCF from snapping out into the cove.

The fundamental concepts underlying elastic instability and their relation to the shape adaptability of the SCF are illustrated in a simplified manner by considering the snap-through behavior of a shallow arch and its load-displacement equilibrium curve (see Fig. 3). The loading history of the shallow arch is shown by the equilibrium curve in Fig. 3a, in which the reaction force F first increases with growing applied displacement u but begins to decrease as the structure softens. When F falls below zero, the structure loses contact with the load-application point and snaps to another equilibrium where $F > 0$ (see Fig. 3b). Similarly, the deformation of the SCF is governed by contact between the SCF and the main wing. As the SCF is pushed into the main wing, it deforms under a controlled

^{††}The slat-gap filler concept is of particular interest to this Paper as it uses a similar thin shell structure.

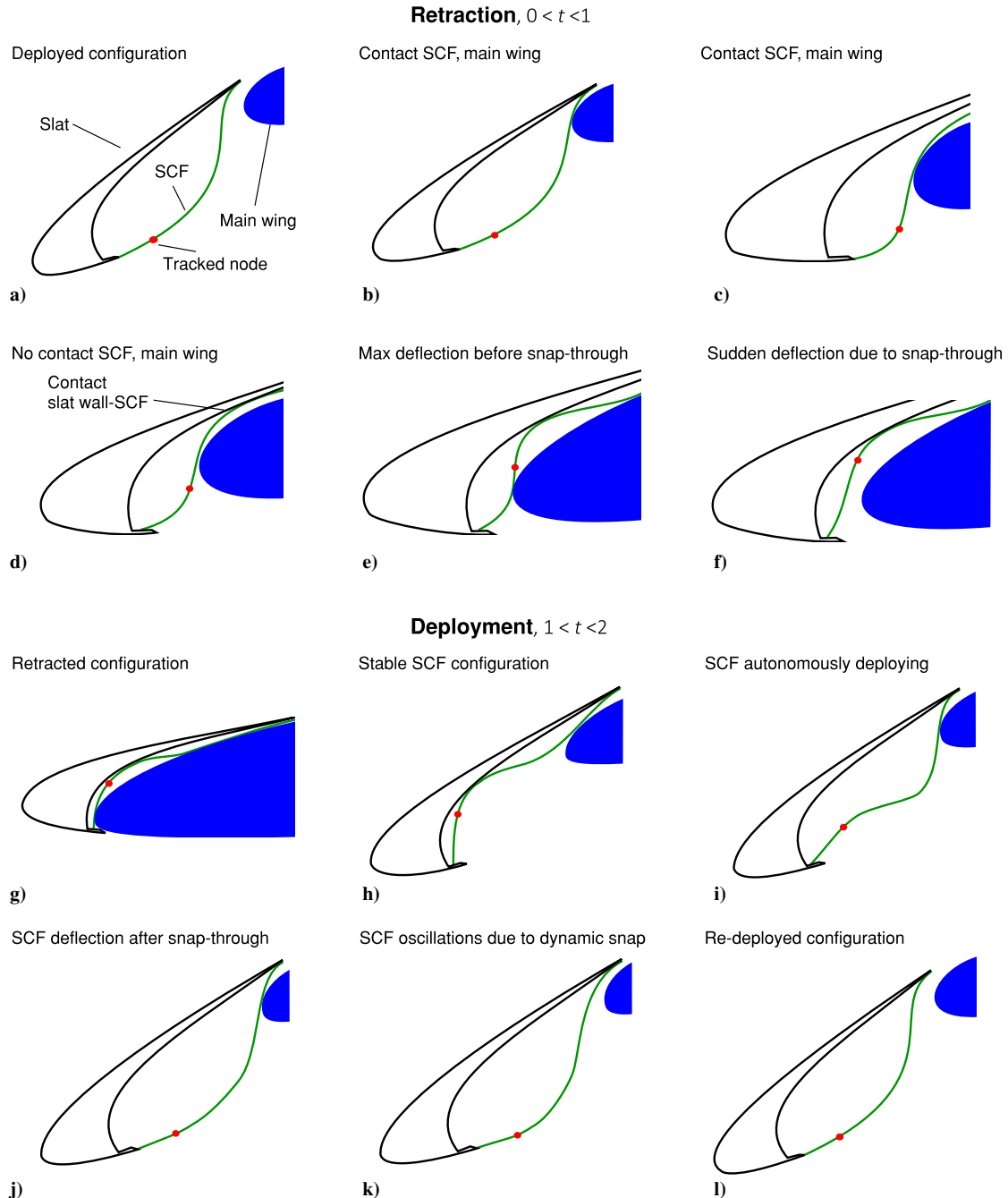


Fig. 2 Retraction a–g) and redeployment g–l) process for a generic SCF due to its interaction with the main wing. The red dot indicates the node used for plotting displacements in Fig. 8.

displacement u with the reaction force at the point of contact F free to modulate, depending on the evolving instantaneous structural stiffness of the SCF. An additional complication, as shown in Fig. 2, is that the point of contact between the SCF and wing changes as the SCF is free to slide along the leading edge of the main wing. Despite this complication, the fundamental nonlinear mechanics driving shape adaptation remain unchanged. Namely, as the SCF only deforms due to the contact with the wing, the SCF loses contact with the wing once the static reaction force becomes negative ($F < 0$). Here, the SCF dynamically snaps through and then restabilizes by contacting the slat-cove wall. This transition in shape across the snap is demonstrated in Figs. 2e and 2f and schematically shown in Fig. 3b.

III. Computational Model Development

This section describes the computational models developed for this Paper. All models are based on a full-scale, freestream-aligned,

high-lift airfoil section extracted from the midspan of the Boeing/NASA Common Research Model (CRM) [41,42]. The models are developed in a similar manner as wind tunnel-scale structure and fluid models from previous work [6,33,36–38]. The geometry employed herein includes an additional SCF profile. For size reference, the retracted chord is 5.1 m, and it is assumed that the SCF is operating in an isothermal environment.

A. Finite Element Structural Model

The full-scale structural finite element model of the CRM wing with attached SCF (shown in Fig. 4a) is built using Abaqus [43], a commercial finite element suite, and is based on wind tunnel scale models developed in previous work [36–39]. The model includes the SCF, leading-edge slat, main wing, and a hinge. The SCF assembly is assumed to be much more compliant than all other components and is modeled as the only deformable body; all other parts are considered

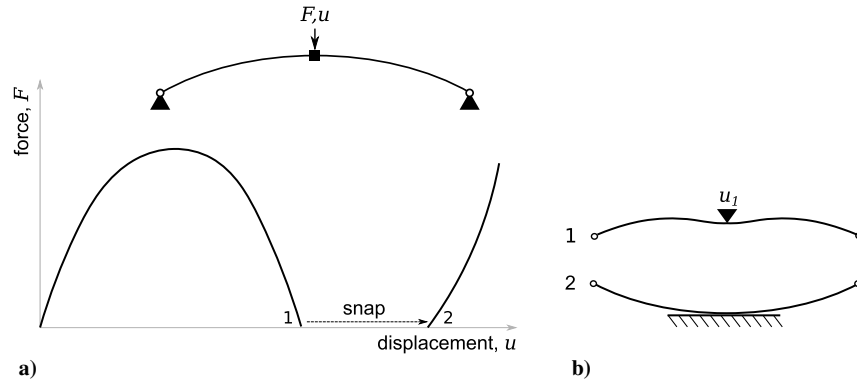


Fig. 3 A shallow arch, representative of a SCF element, which is loaded by a unidirectional displacement u (push only, no pull) at its midspan and resulting in reaction force, F : a) schematic equilibrium manifold showing snap-through when the structure loses contact with the actuation point ($F < 0$) and b) configurations before and after snapping.

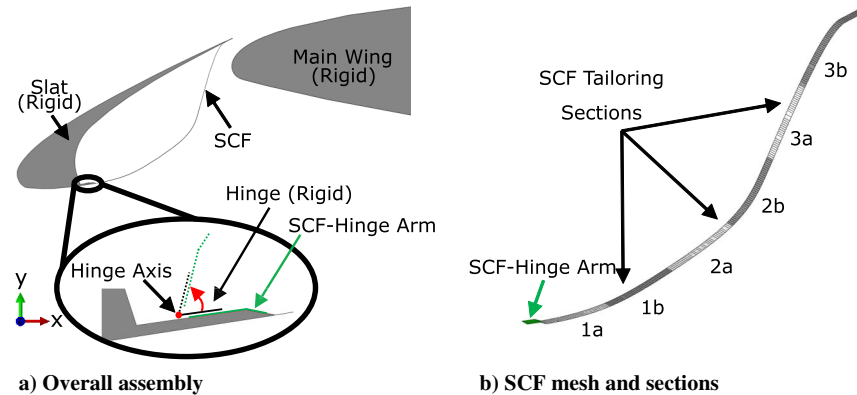


Fig. 4 Structural FEA model of 2.5D SCF assembly: a) schematic of the SCF mounted onto the slat and b) the isolated SCF with sections targeted for thickness and/or layup modification for tailoring of the nonlinear behavior.

rigid. The hinge is connected to the slat and the SCF and is free to rotate, allowing for ease of SCF stowage/deployment (see Fig. 4a). Hinge length (34.6 mm) and position of the hinge axis (18.2 mm from the cove wall) are based on the scaled hinge of a wind tunnel model from previous work [38]. Note that the hinge length is projected onto the SCF (see Fig. 4b). To model an infinitely long SCF in the spanwise (Z) direction and to reduce computational costs, symmetry conditions are applied to edges aligned with the X - Y plane.

As shown in Fig. 4b, the SCF is split into multiple sections including the SCF-hinge arm (assigned steel properties) and six sections of equal length that are modified during the tailoring process. For SMA SCF designs, the tailorable sections are assigned different thicknesses, while for composite SCF designs, these sections are assigned different layups. The material chosen for the composite design studies is E-glass 913, a unidirectional glass fiber epoxy resin system. The SCF is meshed along its curve with 259 equally spaced, reduced-integration shell elements of type S4R. Since the SCF is modeled as infinitely long in the z direction (i.e., using symmetry conditions), it is meshed with one element along the spanwise direction. A linear penetration law models contact in the direction normal to the SCF thickness, while in the tangential direction contact is assumed to be frictionless.

The mechanical responses of the SMA material and E-glass 913 composite lamina is shown in Fig. 5, highlighting both the superelastic behavior of the SMA and the effect of the fiber orientation for the composite. The SMA material initially exhibits a linear stress/strain relationship. Upon reaching a critical stress value, the microstructure transforms from austenite to martensite, allowing for large recoverable deformations [44]. In contrast, the composite material exhibits a linear elastic response with the modulus depending on the fiber direction. Comparing only the elastic response of the two materials, superelastic SMAs appear to be better suited for the large deformations and

snapping behavior associated with the stowage and deployment of the SCF. However, by incorporating elastic instabilities into the composite SCF, an alternative structural superelastic behavior can also be obtained. A significant advantage of exploiting such elastic instabilities is the ability to change system response by both varying geometric and material parameters [10,16]. For this work, the SCF profile cannot be changed because its shape is prescribed for optimal noise reduction. The snap-through response of the SCF is thus modified via stiffness tailoring. An additional possibility would be tailoring the

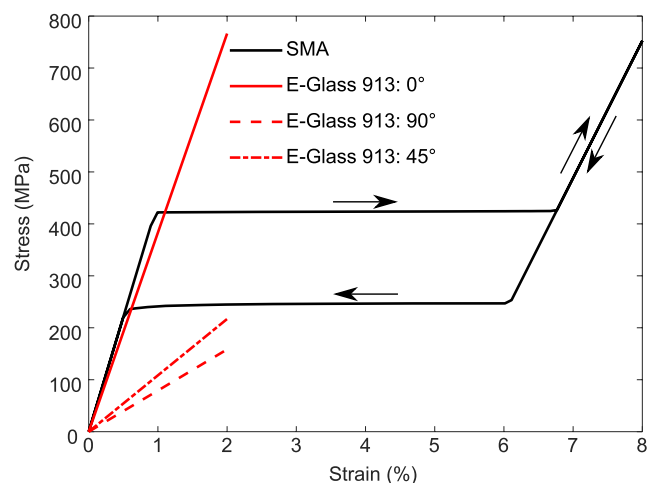


Fig. 5 Superelastic stress/strain response of the SMA material in Table 1 and elastic stress/strain response of E-Glass 913 for various fiber orientations (see Table 2), adapted from [45].

response by prestressing or predeforming the SCF. Practically, this would make the deployed state different in geometry from the manufactured shape and non-stress-free. For simplicity, however, this design option is also not considered in this Paper.

To capture the response of superelastic SMA materials under isothermal conditions, this Paper uses the Souza–Auricchio constitutive model [45], which is particularly useful in collaborative efforts because it is precompiled in Abaqus as a user-material subroutine. Required material properties include elastic modulus; Poisson's ratio; transformation strain H ; critical transformation stresses σ^{Ms} , σ^{Mf} , σ^{As} , and σ^{Af} ; and stress influence coefficients C^A and C^M . Experimental data from isothermal tension tests of SMA material are used to calibrate the material properties of the constitutive model [37]. Table 1 shows the calibrated properties.

Composite SCFs are modeled using the composite lamina feature in Abaqus to create a stack of plies with fibers oriented in different directions. Each lamina within the composite layup has a thickness of 0.125 mm. Properties of the chosen composite material, E-glass 913, are shown in Table 2.

Two sets of load cases are considered during the tailoring process to evaluate each SCF design: 1) six constant aerodynamic loadings using static analysis and 2) a slat/SCF retraction and deployment analysis using an implicit dynamic solver. For the static aerodynamic load case, the slat is fixed in its fully deployed state. The pressure distributions for the aerodynamic loading are extracted from CFD analyses of the CRM wing at 4, 6, and 8 deg angle of attack given Mach 0.20 and Mach 0.24 flow (six total cases), with both the slat and flap in a fully deployed configuration. Note that the Mach 0.20 flow is considered the nominal landing condition and Mach 0.24 flow is considered the most adverse case. For the slat/SCF retraction/deployment load case, aerodynamic loading is not considered because the calculation of pressure distribution on the SCF for different levels of deployment requires an FSI analysis, this more intensive analysis being addressed in Sec. IV. Rotational displacement is applied to the rigid-body reference point assigned to the slat, allowing for control of the slat articulation through a 25.2 deg arc (i.e., full articulation).

Table 1 SMA material properties from [45] (see [46] for definitions)

Property	Value
<i>Elastic properties</i>	
E_A, E_M	44.9 GPa, 26.4 GPa
$\nu_A = \nu_M$	0.33
<i>Phase diagram properties</i>	
σ^{Ms}, σ^{Mf}	422 MPa, 425 MPa
σ^{As}, σ^{Af}	247 MPa, 231 MPa
$C^A = C^M$	7.12 MPa/K
<i>Transformation strain properties</i>	
H	5.15%
<i>Other properties</i>	
ρ	6480 kg/m ³

Table 2 E-Glass 913 layer properties

Property	Value
ρ	1900 ^c kg/m ³
E_1, E_2	38.7 ^d GPa, 8 ^d GPa
ν_{12}	0.28 ^d
X_c^a, Y_t^b	1548 ^d MPa, 65.5 ^c MPa
X_c^a, Y_c^b	1000 ^d MPa, 150 ^d MPa
S	40 ^d MPa

^aFibers direction 0 deg.

^bFibers direction 90 deg.

^cBased on Hexcel data.

^dBased on [47,48].

B. Finite Volume Fluid Model

The finite volume fluid model of the CRM wing in flow is built using SC/Tetra [46], a thermofluid finite volume solver that has a precompiled link to the Abaqus Co-Simulation Engine [43]. The fluid model shown in Fig. 6 consists of a rectangular fluid domain centered around the CRM wing, the domain being 20 chords long in the flow direction and 14 chords high in the vertical direction. To reduce computational cost and maintain consistency with the structural model, the fluid model is meshed with a single element in the spanwise direction. A single fluid mesh is not sufficient for this problem due to the large volume change associated with SCF deformation and the rigid-body motion of the flap and slat. Instead of performing multiple remeshes of the entire fluid model, this Paper uses an overset mesh scheme [38,46] that subdivides the fluid domain into two deformable and movable slave meshes (one tracking each articulating high-lift device) and a master mesh (the main wing and remaining fluid volume).

The fluid domain containing the main wing and overall flowfield is defined using multiple volume regions assigned different element sizes, those near the wing having a more refined mesh as compared to freestream volumes farther away from the wing. The volume regions associated with the slat and flap are meshed with the same element size as the innermost region of the master mesh. The mesh is further refined at the surface of the wing where layers of hexahedron elements are also inserted, increasing the resolution of the flowfield to capture the boundary layer. Previous CFD work at the wind tunnel model scale of the CRM wing serves as a basis for the mesh generation parameters in the current work [37]. After combining the three meshes, the resulting fluid model has approximately 850,000 elements (805,000 prism and 45,000 hexahedron elements).

The fluid domain is assigned incompressible air properties with viscosity and density of $1.83 \cdot 10^{-5}$ Pa . . . and 1.206 kg/m³, respectively. Turbulent characteristics of the flow are captured using the shear-stress transport $k - \omega$ turbulence model [47], which is accurate both in the far field and near the surface of the walls. Boundary conditions for the fluid model consider the existence of an inlet, an outlet, and walls. Inlet conditions are applied on the left and lower surfaces of the outermost volume region, where the x - and y -components of the inlet velocity [magnitude of either Mach 0.20 (68 m/s) or Mach 0.24 (82 m/s)] are specified. The angle of attack for the wing is defined by the specification of the inlet velocity components. This allows the same CFD mesh to be used for all considered flow conditions. Additionally, the flow through the inlet is assumed to be approximately laminar, and thus the turbulent kinetic energy k and turbulent dissipation rate ϵ are set to approximately laminar values of 0.0001 m²/s² and 0.0001 m²/s³ [46]. The outlets for the fluid model (0 Pa static pressure) are specified as the upper and right boundaries of the outermost fluid region. Smooth no-slip and no-penetration wall conditions are assigned to every surface of the wing, deformable or rigid.

Transient CFD analysis is conducted for each flow condition (4, 6, and 8 deg angle of attack with freestream conditions of Mach 0.20 and Mach 0.24) with a total time of 3 s using a time increment of $5 \cdot 10^{-5}$ s to develop the flow to approximately steady conditions.^{‡‡} The time-averaged (approximately steady) pressure distribution on the SCF is extracted from each analysis and used for aerodynamic loading cases during the structural tailoring process. These CFD analyses are also used as initial conditions for the fluid model during the FSI analyses.

C. FSI Framework

FSI analysis is required to both assess the viability of SCF designs obtained via the tailoring process and understand how each design behaves in fluid flow. For FSI analysis, structure and fluid solvers are coupled using the Abaqus Co-Simulation Engine. The coupling

^{‡‡}Transient analysis, conducted until steady conditions are reached, is chosen instead of a steady CFD analysis because flow features generated by the high-lift configuration, such as separation on the upper surface of the flap, prevented a steady-state solution.

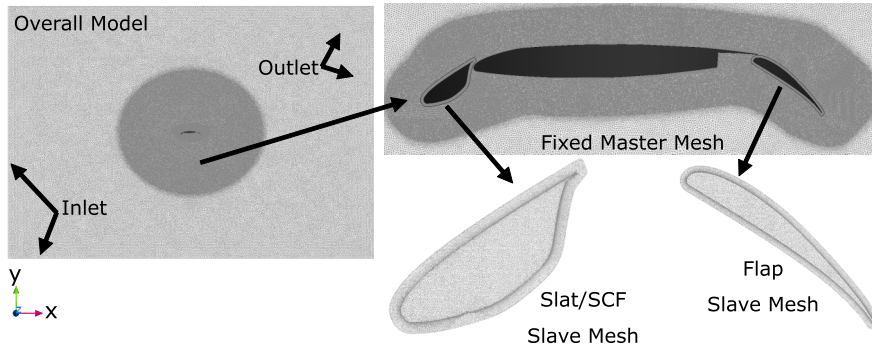


Fig. 6 Fluid model of the CRM wing.

scheme employs a Gauss–Seidel time incrementation, whereby each solver calculates its respective physical quantities separately, transferring relevant data to the other solver at set time increments across a shared interface (i.e., the outer mold line of the slat/SCF). Abaqus transfers the displacement of the slat/SCF (either from deformation or rigid-body motion), while SC/Tetra provides the pressure loading applied to the slat and SCF. Note that the framework is only compatible with transient CFD and finite element analysis (FEA) solvers; thus, static FSI analysis is not possible. Additionally, aside from numerical damping native to both solvers, no structural or numerical damping is explicitly defined. This is deemed reasonable, as other sources of damping that may affect the SCF have not been quantified and further study of these sources is beyond the scope of this Paper.

Similar to the structural evaluation of each SCF design, FSI analysis is split into two cases. The first case considers the high-lift devices in fixed, fully deployed configurations. The continuous deflection of the SCF, both the mean quantity and potential oscillations, is of interest for this load case. The second case is retraction and deployment of the high-lift devices. Slat articulation is controlled by Abaqus (see Sec. III.A), while rigid-body motions defined in SC/Tetra are sufficient to describe the flap. During high-lift device articulation, the closed volume mesh of the slat-SCF assembly undergoes significant deformation (e.g., element volume reduction during retraction), eventually creating zero-volume elements. To avoid these, a previously developed slat/SCF remeshing scheme is implemented [38] that pauses FSI analysis at a specified time, extracts and rebuilds the deformed slat/SCF mesh, and then reinserts it into the fluid model. FSI analysis is then continued.

D. Tailoring Process Constraints

1. Displacement from Aerodynamic Loading

When deployed and under aerodynamic loading, the SCF must not significantly deform; previous work [20,25] has shown that the SCF shape employed here is the most effective for noise mitigation and significant displacement of its surface may reduce this effectiveness. Additionally, large deviations from the optimal SCF shape may lead to structural oscillations and perhaps additional noise. Based on previous work on the full-scale CRM SCF [48], here we assume a maximum displacement of 3.4 mm; a tailored composite SCF design is considered infeasible if it fails to meet this constraint for any of the six aerodynamic loading conditions.

2. Composite Stress Analysis

During the retraction process, the SCF is subjected to large deformations and associated high strains that can lead to possible material failure. The common Tsai–Wu failure criterion (TWFC) [49] is used herein to assess potential failure in the composite SCFs. It accounts for interactions between different stress components and has been shown to provide good failure predictions for composites [50].

According to the TWFC, for a state of plane stress, the failure index I_F of an orthotropic lamina is

$$I_F = F_1\sigma_{11} + F_2\sigma_{22} + 2F_{12}\sigma_{11}\sigma_{22} + F_{11}\sigma_{11}^2 + F_{22}\sigma_{22}^2 + F_{66}\sigma_{12}^2 \quad (1)$$

where σ_{11} and σ_{22} are the stress components longitudinal and transverse to the fiber direction, respectively, and σ_{12} is the in-plane shear stress. The F coefficients in Eq. (1) are given by

$$\begin{aligned} F_1 &= \frac{1}{X_t} - \frac{1}{X_c}, & F_2 &= \frac{1}{Y_t} - \frac{1}{Y_c} \\ F_{11} &= f^* \sqrt{F_{11}F_{22}}, & F_{12} &= \frac{1}{X_t X_c} \\ F_{22} &= \frac{1}{Y_t Y_c}, & F_{66} &= \frac{1}{S^2} \end{aligned} \quad (2)$$

where X_t , X_c , Y_t , and Y_c are experimentally determined material failure strengths in uniaxial tension t and compression c in the directions longitudinal X and transverse Y to the fibers and are summarized in Table 2 for E-Glass 913. The in-plane shear strength S and all five experimental failure strengths in Eq. (2) are assigned positive quantities. The value of the normalized interaction term f^* is not easy to determine accurately with experiments. A value of $f^* = -0.5$ is used herein, based on recommendations found in the literature [50].

The TWFC is applied to each k th lamina in the composite SCF and checked at multiple locations along its arc length s such that $I_F^k = I_F^k(s)$. To prevent local failure at any point in the composite laminate, the failure index needs to satisfy

$$\max_{k \in [1, N]} I_F^k(s) < 1 \quad (3)$$

where $k \in [1, N]$ spans the laminae in the composite stack.

Composite laminates are particularly prone to delamination, necessitating calculation of interlaminar stresses. As plane stress shell elements are used in the structural models, accurate interlaminar stresses are not available from Abaqus directly. Thus, these stress components are derived via postprocessing of the in-plane values, σ_{xx} and σ_{xy} , using Cauchy's indefinite equilibrium equations with a postprocessing technique described in [51],

$$\sigma_{xz}^k(z) = \sigma_{xz_b}^k - \int_{z_b}^z (\sigma_{xx,x} + \sigma_{xy,y}) dz \quad (4)$$

where $\sigma_{xz_b}^k$ is the interlaminar shear stress at the bottom of the k th layer and equal to zero at the bottom and top layer of the composite; σ_{xx} and σ_{xy} are extrapolated from Abaqus simulations. To prevent delamination, $\sigma_{xz}^k(z)$ at each layer interface $\sigma_{xz_b}^k$ must be less than the shear strength of the resin that bonds the laminae.

IV. Designing Nonlinear SCF Behavior: Mechanical and FSI Evaluations

In this section, results of the structural design process are presented, and those from FSI analyses on multiple SCF designs in realistic flow conditions are discussed.

A. Structural Design Methodology of SCF

An ideal SCF design releases little kinetic energy KE during the retraction snap-through (slat moving toward the main wing), reducing the severity of impact between the SCF and slat, and stores little strain energy SE when fully retracted, decreasing the actuator loads required to articulate a slat with a SCF. Simultaneously, a high release of KE and high reaction force is desired during deployment snap out as these can be associated with full deployment even in the presence of aerodynamic pressure fields. To achieve this behavior, improve structural performance, and satisfy the imposed constraints described in Sec. III.D, the nonlinear structural retraction process of the SCF is investigated.

Previous work has focused on the application of SMA materials to the SCF [6]. Here, lightweight composite materials are considered for the first time. Compared to SMA-based designs, the lower material density and cost of the glass fiber composite provide an advantage, while their manufacturing process also enables elastic tailoring. Obtaining different ply stacking sequence solutions permits control of the equilibrium manifold and, consequently, tailoring of the retraction deployment as needed.

The design of the composite SCFs is carried out via a trial-and-error methodology as the stacking sequence is modified along the SCF arc length. Note that this process can be generalized to apply to SMA SCF designs. The design procedure can be described as follows:

1) A core stacking sequence (denoted by $[C]$), which satisfies material failure requirements (see Sec. III.D) is chosen based on preliminary structure evaluations. These evaluations showed that stacking sequences with alternating layers between ± 45 and 90 deg consistently exhibited matrix-dominated failure in the dominant strain direction (along the arc length of the SCF) due to the lack of reinforcing fibers. Subsequently, stacking sequences with alternating ± 15 and ± 30 deg layers were found to satisfy the failure and transverse shear stress delamination constraints (see Fig. A2), while providing sufficient strength in the spanwise direction of the SCF, leading to the selection of the core stacking sequence.

2) This core layout is then modified parametrically by adding/removing 0 deg layers along the SCF arc length (in the six tailoring subsections) such that the maximum displacement requirement (Sec. III.D) for the six static aerodynamic loadings is still satisfied. This enables tailoring of the nonlinear response to achieve a variety of behaviors and equilibrium manifolds, including desirable responses such as low stored SE and low release of KE during retraction. Note that the 0 deg layers are only added on the top and bottom of the core sequence as here strains are too high for matrix-dominated layers in the longitudinal direction.

3) Finally, the nonlinear structural response of the retraction and redeployment process for a SCF design is assessed via finite element structural analysis, allowing for the study of how various physical features, such as released and stored energies and reaction forces, affect the nonlinear behavior of the SCF.

Ideally, during the tailoring of the nonlinear SCF behavior, each design would be evaluated using FSI analysis with two load cases described in Sec. III.C (i.e., two additional steps to the previously mentioned design methodology): 1) fixed, fully deployed and 2)

deployment. However, because of the time associated with assessing a single design via FSI analysis (approximately 3.5 days on a standard workstation with ten cores for each load case), this is not feasible. Instead, a number of designs are developed via the mentioned procedure, but only a few are later evaluated using FSI analysis in Secs. IV.C and IV.D.

To demonstrate the variety of nonlinear responses achievable via this design methodology, five composite SCFs are developed (see layouts in Table 3). Composite-m is a monolithic, uniform-thickness, composite baseline design, while composite-t1 to composite-t4 are tailored designs. Figure 7 shows a schematic of the ply orientations for the composites core $[C]$ and composite-t1. Note that the section designations correspond to the chordwise sections indicated in Fig. 4b.

Given the general applicability of the design approach, we also apply it to the SMA SCF. Starting from a baseline monolithic SMA SCF (SMA-m) with the minimal thickness required to satisfy the deflection constraint of 3.4 mm under the considered aerodynamic conditions, SMA thicknesses along the SCF arc length in the six tailoring subsections are varied. In this Paper, we present a single tailored SMA SCF design (SMA-t). Table 3 shows the distribution of thickness for both SMA designs.

B. Structural Analysis of SCF Designs

Figure 8 shows the nonlinear behavior of two SCF designs (SMA-m and composite-m) during the retraction/deployment process depicted in Fig. 2. Figures 8a and 8b show the deflection δ of the node indicated by the red dot in Fig. 2 plotted against force F , defined as the sum of the reaction forces measured at the forward and aft ends of the SCF (i.e., hinge and tie joint with the slat, respectively). Figure 8c shows the area-specific kinetic energy KE released at the same tracked node, which is defined as

$$KE = (1/2)v_n^2 \rho h \tag{5}$$

where v_n is the velocity of the node indicated by the red dot in Fig. 2, ρ is the material density, and h is the thickness of the SCF at the position of the node. The node for area-specific kinetic energy calculation is within the section of the SCF critical for snapback (autonomous deployment) for a design. Note that a global kinetic energy quantity would include dynamic events away from this point and therefore provide misleading quantities. Shown in Fig. 8d, the strain energy, however, is computed over the entire SCF as it signifies the energy input required by the slat actuation system to stow the SCF.

As illustrated in Fig. 8a, once the SCF contacts the main wing, the force F increases until the deformation of the SCF reduces the force to a minimum of 4.7 N for the SMA-m design and 15.3 N for composite-m. The corresponding deflection for the minimum force for both designs is approximately 0.48 m. Note that the sudden decrease in force between 0.45 and 0.5 m coincides with a temporary loss of contact between the SCF and the main wing, leading to a dynamic snap of the SCF until it contacts the slat-cove wall (see Fig. 2d). Once contact with the wing is reestablished (see Fig. 2e), F increases as the SCF is further deformed by the wing. Because of the simultaneous geometric and constitutive superelastic effects, the

Table 3 Ply properties, stacking sequences, and thickness distributions along the SCF arc length

Sample	Section 1a	Section 1b	Section 2a	Section 2b	Section 3a	Section 3b
CORE $[C]$	[(0) ₂ / ± 15/ ± 30/ ± 15/0] ₂					
Composite-m	[(0) ₂ /[C]/(0) ₂]					
Composite-t1	[0/[C]/0]		[(0) ₂ /[C]/(0) ₂]			
Composite-t2	[C]	[0/[C]/0]	[(0) ₂ /[C]/(0) ₂]			
Composite-t3	[C]	[C]	[(0) ₂ /[C]/(0) ₂]			
Composite-t4	[C]	[(0) ₂ /[C]/(0) ₂]				
SMA-m	Thickness = 2.25 mm					
SMA-t	Thickness = 2.18 mm				Thickness = 2.32 mm	

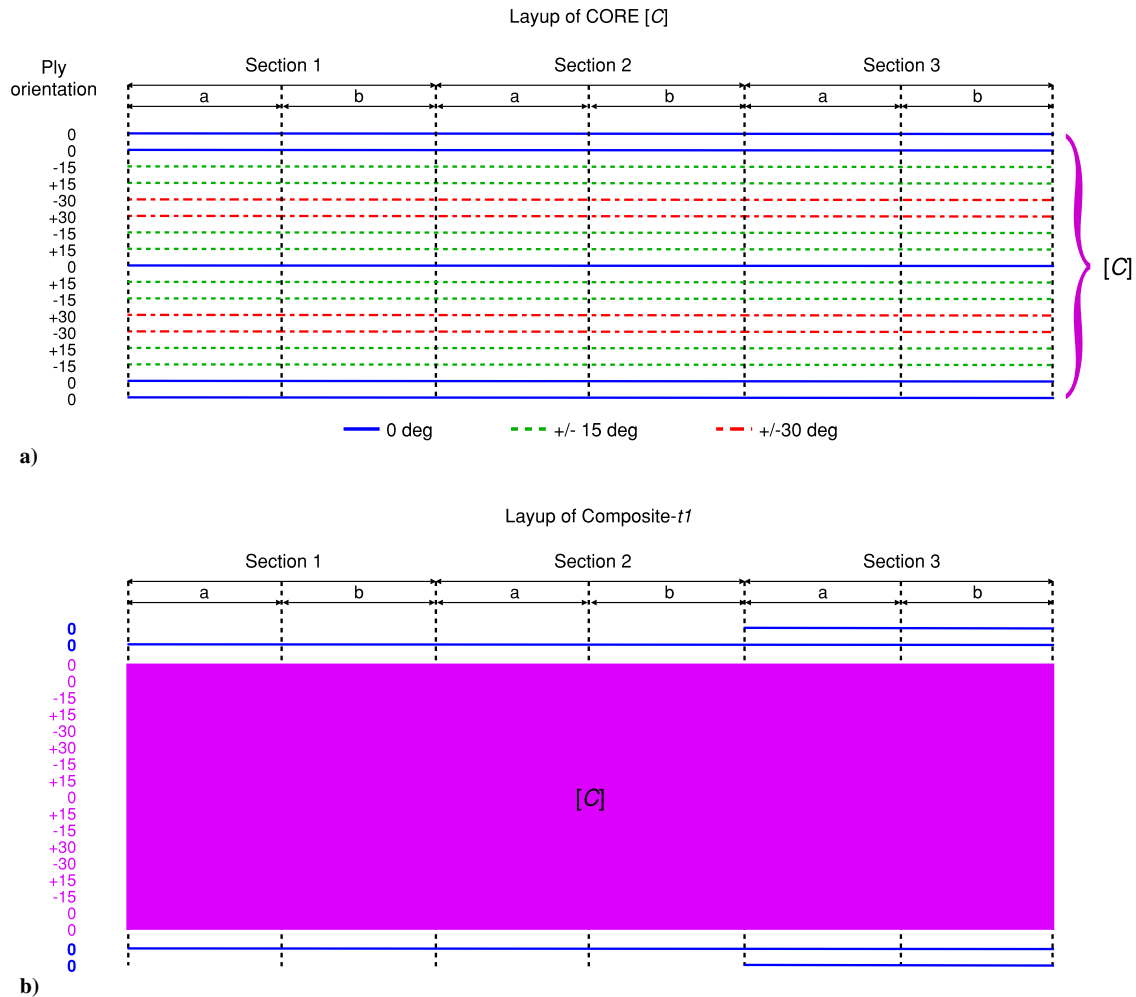


Fig. 7 Stacking sequence and thickness variation of fiberglass SCF: fiberglass SCF: a) lines represent composite layers and fiber orientation of the CORE [C], and b) shows composite-t1 where plies of 0 deg are added along the SCF arc length on top and bottom of [C]. Step changes in thickness cause stiffness variations in the structural asymmetry required to tailor the snap-through and snapback events.

strain energy in the SMA-m design remains relatively constant, while the strain energy in the composite-m design increases.

Final snap-through of the monolithic composite and SMA designs into the stowed configuration corresponds to a dynamic jump in the F vs δ curves of Fig. 8a. As shown in Figs. 8c and 8d, the snap-through causes a sudden peak of area-specific kinetic energy and a corresponding drop in strain energy. Figures 8b and 8d show that during SCF redeployment, after an initially smooth reduction in reaction force and strain energy, both quantities remain relatively constant for the SMA-m (due to its material constitutive properties) and gradually reduce for the composite-m as the SCF remains in its stowed state (see Figs. 2h–2l for reference). As the point of contact between SCF and main wing slides to the aft end of the SCF, at a deflection of 0.1 m, spontaneous snapback is triggered. This corresponds to largest peaks in force (Fig. 8b), a drop in strain energy (Fig. 8d), and sudden release of kinetic energy (Fig. 8c). It is worth noting that, even though composite-m stores more SE during the retraction phase, the SMA-m exhibits a larger release of KE due to its higher density. With regard to the monolithic SCF designs, these results suggest that the SMA-m exhibits a more efficient structural performance compared to the composite-m, as it causes less severe impact between SCF and slat wall and a reduction in actuation energy. Chances of redeployment in fluid flow appear to be similar. While SMA-m shows high values of KE related to its density, composite-m compensates with higher reaction forces during snapback.

Figure 9 summarizes the structural behavior during the retraction and redeployment stages for the tailored SMA (SMA-t) and tailored composite-t1, composite-t2, composite-t3, and composite-t4 SCF designs. Results show that the tailoring of the SCF under constraints

leads to a range of dynamic responses. As seen from the force vs deflection curves in Figs. 9a and 9b, the tailored designs show qualitatively similar behavior to the monolithic designs in Figs. 8a and 8b. However, during retraction, composite-t2, composite-t3, and composite-t4 show earlier snap-through into the stowed configuration due to variable stiffness between Secs. I and II. Additionally, all designs show smoother equilibrium curves, indicating a more gradual retraction and deployment process. As a result, there are significant reductions in maximum strain energy (-10.5%) and snap-through kinetic energy (-44.4%) compared to the SMA-m design (see Figs. 9c and 9d), demonstrating the effectiveness of the adaptation-by-instability approach. Snapback into the redeployed configuration occurs at approximately the same instant (approximately 1.85–1.87 s or 90% slat deployment) for all designs, when the SCF has moved sufficiently along the main wing, enabling it to freely snapback into a redeployed configuration. The tailored SMA design shows the lowest release of kinetic energy during the stowage, minimizing the risk of potential damage due to collisions with the slat. This is likely due to the combined superelastic behavior of material and geometric nonlinearities. Composite-t3 also shows a reduced release of area-specific KE and actually snaps twice due to interactions with the main wing and the slat, thereby releasing kinetic energy more gradually across two dynamic events.

With regard to redeployment of the SCF in flow, most of the tailored designs show large values of KE at the end of the deployment process, indicating a greater chance of successful redeployment in flow as compared to the monolithic composite design. However, the KE during snapback of all tailored designs is less than the monolithic SMA design (see Table 4), which remains the most likely design to

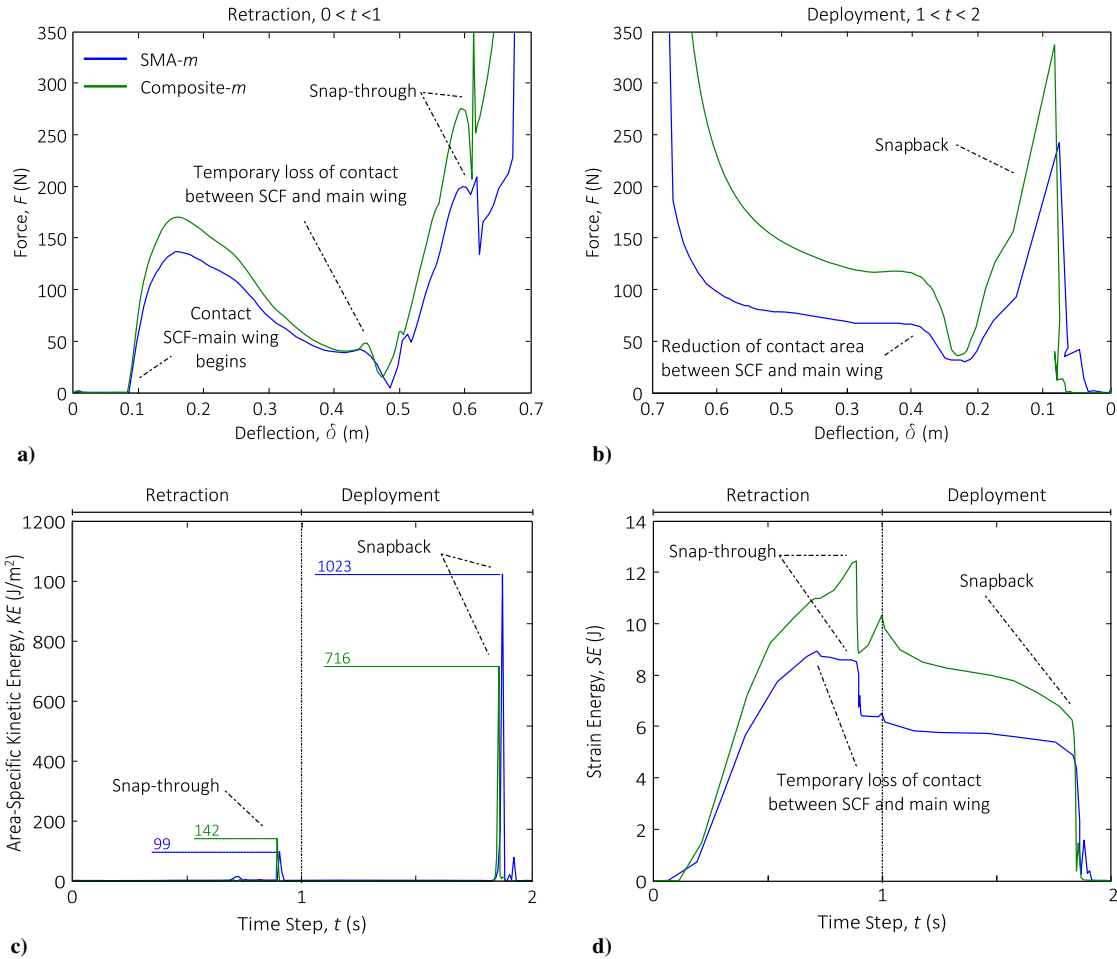


Fig. 8 Nonlinear force vs deflection dynamic behavior during a) SCF retraction and b) redeployment of the SMA-m and composite-m monolithic designs. The associated release of specific kinetic energy and stored strain energy are plotted in c) and d), respectively.

redploy in flow. Another metric for judging the likelihood of snapback under aerodynamic loading is the force F , measured as the sum of reaction loads at the forward and aft ends of the SCF after snapback, as this quantifies the intensity of the snap. As shown in Fig. 9b (and summarized in Table 4 as peak F at snapback), of the tailored designs, SMN-t and composite-t4 exhibit the greatest peaks in force during snapback and are therefore most likely to redeploy under the external influence of dynamic aerodynamic pressure. Of all composite designs, composite-t2 is least likely to redeploy as both the released KE (Fig. 9c) and peak support force (Fig. 9b) are the lowest. In summary, all the design solutions, monolithic and tailored, show a monostable nonlinear response as when the slat separates from the main wing the SCF autonomously redeploy (in the absence of airflow). Modification of the SCF thickness/layout allows for tailoring of the nonlinear dynamic responses, thereby providing a design tool to achieve an efficient and predictable structural behavior without modifying the geometry of the SCF.

These important model responses are summarized in Table 4. The results show that all tailored composite designs reduce the strain energy required to induce snap-through as compared to the monolithic composite design and that all designs pass the TWFC and peak interlaminar shear stress constraints. The design with the lowest peak strain (and perhaps the greatest durability) is composite-t2, while composite-t1 and composite-t3 show low kinetic energy at snap-through and high kinetic energy at snapback. However, the peak support force of composite-t1, composite-t2, and composite-t3 is significantly lower than for composite-t4 and SMN-t.

C. Fluid/Structure Interaction: Fixed, Fully Deployed

As stated in Sec. IV.A, the tailoring process for the nonlinear behavior of both the SMA and composite SCF designs only considered:

1) constant pressure loads on the fully deployed SCF and 2) retraction/deployment under no pressure loading. Understanding the true behavior of the flexible SCF in dynamic fluid flow and, in turn, assessing the viability of designs obtained by the tailoring process, requires full FSI analysis.

The first FSI load case assumes that the slat is fixed such that both slat and SCF are fully deployed. As previously stated in Sec. IV.A, a limited number of SCF designs are considered for FSI analysis: 1) monolithic SMA, 2) tailored SMA, 3) tailored composite-t2, and 4) tailored composite-t4. Additionally, each SCF design is only evaluated using the flow condition that resulted in the highest deflection from static FEA analysis. This flow condition is Mach 0.24 at 8 deg angle of attack for composite SCFs and Mach 0.24 at 4 deg angle of attack for SMA SCFs. The difference in flow conditions may be due to the larger variation in stiffness along the curve of the composite SCFs as compared to SMA SCFs. Each analysis is conducted for 2.5 s with a time step of 5×10^{-5} s.

Figure 10 shows the deflection (displacement magnitude) of the node in each structural model with the maximum displacement during the analysis for each of the SCF designs considered. All FSI-predicted displacements exhibit an oscillatory behavior with an initially high amplitude due to the sudden imposition of flow on the structure. For all designs except composite-t4, this oscillatory behavior decays toward a smaller constant amplitude. It is expected that in a longer analysis the SCF may reach a steady equilibrium configuration with the surrounding fluid for these cases. Instead of only showing the steady-state response, the initial oscillatory response and subsequent decay are shown to demonstrate how each SCF design behaves within the same time span, providing an indication of how fast a design could return to steady state when perturbed. Both the composite-t2 and SMN-t designs tend to stabilize

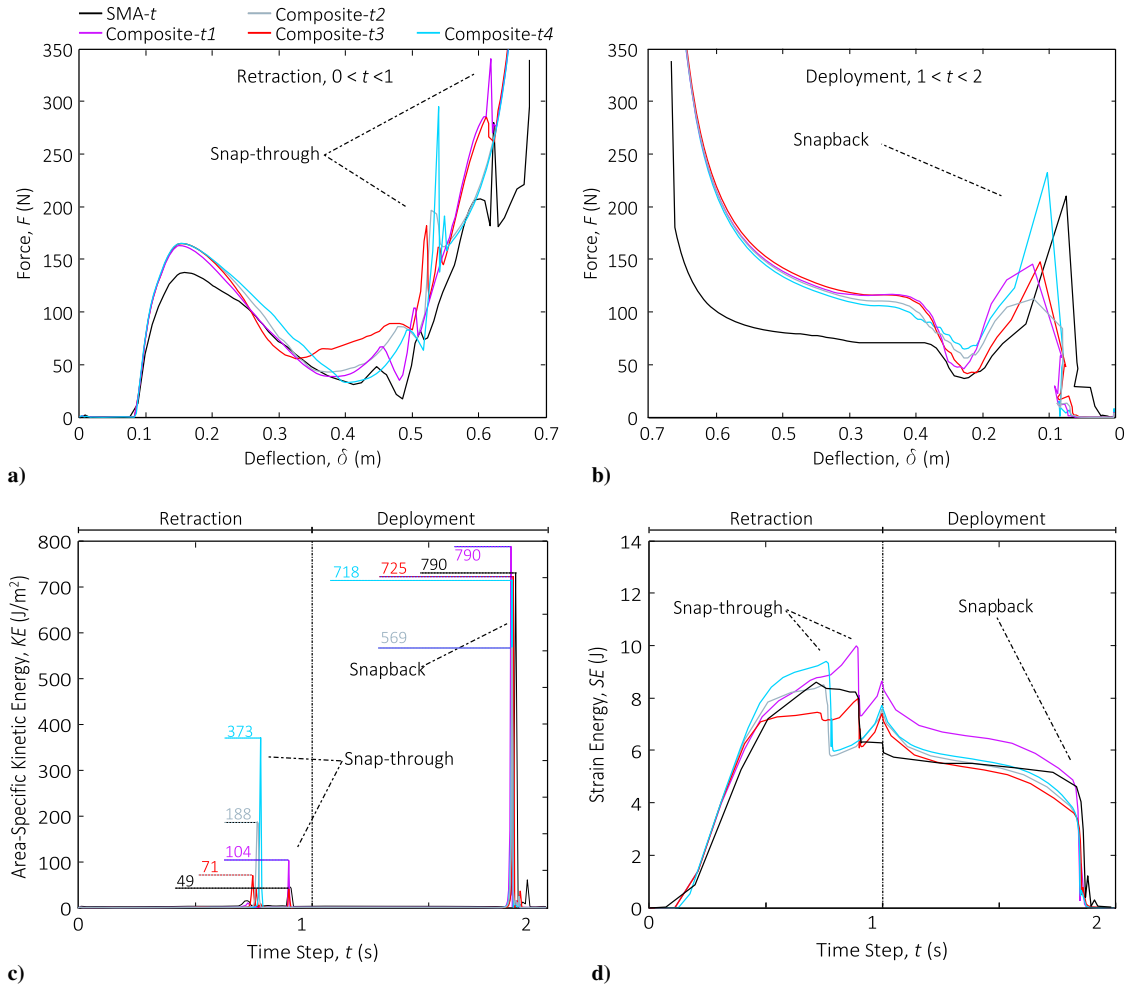


Fig. 9 Force vs displacement plots of a) the retraction and b) redeployment events of the tailored SMN-t and tailored composite-t1, composite-t2, composite-t3, and composite-t4 SCF designs. The corresponding c) released kinetic energy and d) stored strain energy during the actuation processes are plotted vs time.

Table 4 Comparison of different SCF designs with SMA and composite material solutions

Material	Material density ρ , kg/m ³	Kinetic energy at snap-through and snapback KE_{st} , KE_{sb} , J/m ²	Strain energy at snap-through SE_{st} , J	Peak F at snapback F , N	Max strain ϵ_x , %	TWFC I_P^k (s)	Interlaminar shear stress σ_{xz} , MPa
SMA-m	6480	99, 1023	8.94	243	-1.60	—	—
SMA-t	6480	49, 731	8.59	211	-1.56	—	—
Composite-m	1900	142, 716	12.48	338	-1.68	0.82	-6.25
Composite-t1	1900	104, 790	10.02	146	-1.58	0.86	-5.42
Composite-t2	1900	188, 569	8.53	113	-1.33	0.86	-3.94
Composite-t3	1900	71, 725	8.00	148	-1.47	0.89	-4.26
Composite-t4	1900	373, 718	9.43	233	-1.49	0.86	-4.37

faster as compared to the monolithic and tailored composite-t4 designs, the latter showing unacceptable instability. Additionally, unlike other designs, composite-t4 exhibits significant oscillation about two points (see Fig. 10d) with similar frequencies that are approximately in the same locations as the maximum deflections for the other SMA and composite designs. The amplitude of the oscillations for composite-t4 are large enough such that the two points exhibit the highest deflection at different times, unlike composite-t2 (see Fig. 10c).

Additionally, shown in Fig. 10 are the calculated displacements at these same nodes from FEA considering two static pressure fields: 1) pressure from the initial CFD analysis (which establishes flow conditions for FSI analysis) and 2) time-averaged pressure from FSI

analysis. It can be seen that the resulting nodal displacement from the static analysis with the time-averaged FSI pressure distribution is approximately equal to the time-averaged displacement from the FSI analysis, as expected. With the exception of composite-t4, the displacement of the structure calculated using the initial CFD pressure distribution is significantly lower, indicating an adverse pressure-deflection relationship.

Displacement of the entire SCF, instead of the one node with maximum deflection, is examined to better understand the trends in Fig. 10. The static deflection of the SCF tends to be toward the cove in and near sections 1b and 3a in Fig. 4 and away from the cove in and near section 2b. Static deflection in the SCF creates stress in the structure that affects the dynamic response, and in turn, the deflected

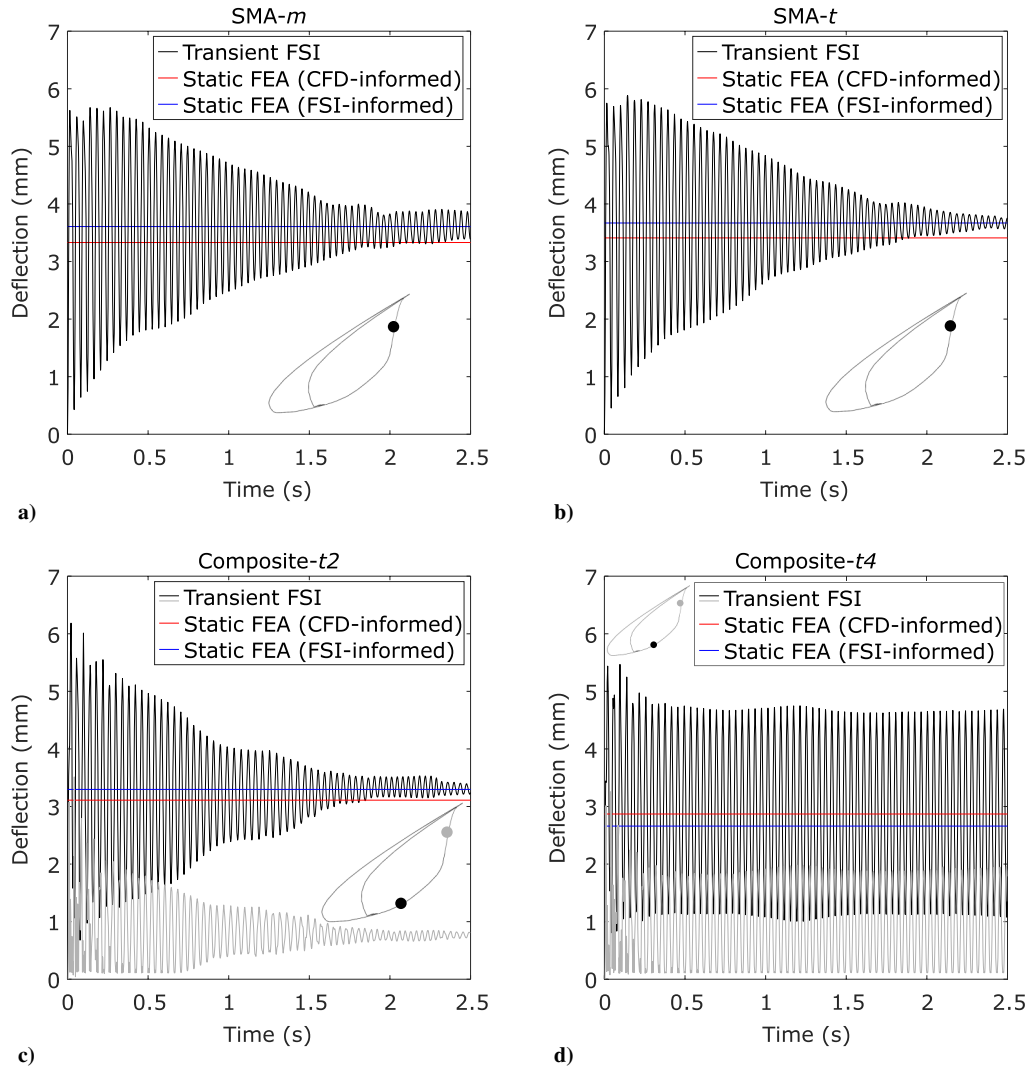


Fig. 10 Deflection time histories for points of highest displacement given four different SCF designs: a) monolithic SMA, b) tailored SMA, c) tailored composite-t2, and d) tailored composite-t4. Deflections from static FEA using the time-averaged FSI pressure field (blue) and initial CFD pressure field (red) are also shown.

shape affects the pressure distribution developed by the fluid flow. For all designs except composite-t4, the aerodynamic pressure increases with larger deflection into the cove and away from the undeformed shape. This effect accounts for the FSI-informed static deflection being greater than the CFD-informed in Figs. 10a–10c. Additionally, stress relief in the structure and decreasing aerodynamic pressure cause the dynamic deflection response to be asymmetric, favoring lower deflection until a solution time of about 0.5 s.

For the composite-t4 design, opposite trends are observed such that the aerodynamic pressure decreases with increasing deflection of the SCF into the cove from the undeformed configuration. This opposite trend accounts for the FSI-informed static deflection being less than the CFD-informed solution in Fig. 10d. Similarly, asymmetric dynamic deflection response that favors larger deflections is noted. However, in the composite-t4 design, the dynamic deflection response shows no indication of decrement or ringdown. These trends suggest that, while the difference in layup between the two composite designs is small, the particular stiffness and mass distribution of the composite-t4 design couple to the aerodynamics in an undesirable manner.

Based on the results of the FSI analysis and static FEA, only the composite-t2 design still satisfies the displacement constraint while remaining stable during FSI analysis. Overall, these results suggest that coupling between the pressure field and the displacement of the SCF tends toward destabilization of the SCF, further reinforcing observations from previous work [48]. As the SCF is deformed due

to aerodynamic loading, the local pressure field changes such that the SCF displaces further. Note that, while this behavior is undesirable, the Mach 0.24 flow speed is the most adverse condition. Under nominal Mach 0.20 flight conditions, the SCF has a lower displacement and is thus less affected by this destabilizing coupling. These results demonstrate that the coupled FSI response must be considered in the design of the SCF to result in acceptable performance.

D. Fluid/Structure Interaction: Deployment

The second load case assumed for FSI analysis considers transient deployment of the slat and SCF, critical because any viable tailored SCF designs must redeploy under dynamic flow conditions. For each SCF design analyzed, an initial structural analysis (no aerodynamic loading) is performed to fully retract slat and SCF. The resulting assembly geometry is extracted and used to generate a slave mesh for the overset fluid model (see Sec. III.B). This approach for obtaining the SCF retracted geometry is chosen because the flow conditions change between landing and takeoff (requiring another set of FSI analyses), and during retraction, the SCF deformation is dominated by contact between the main wing and the slat. Additionally, once fully retracted, the SCF is cut off from the flowfield. Similar to the previous FSI load cases, initial conditions for the FSI deployment analysis are developed by performing a CFD analysis. Far-field flow conditions are identical to the previous FSI load case (i.e., Mach 0.24 and the same angles of attack). Because the SCF is cut off from flow and in contact with the main wing, the initial oscillations at the start of

FSI analysis (similar to those in the fixed, fully deployed FSI cases) are not expected. However, oscillatory behavior could be induced during slat deployment as the SCF is reintroduced to the flow and due to inertial effects from deployment (snapout). During the FSI analysis, both the slat and flap are synchronously deployed over 2 s with a time step of 5×10^{-5} s and then held in a fully deployed position for 0.5 s resulting in a computational cost of approximately 3.5 days on a standard workstation with ten cores. Note that the deployment of the slat and flap in this analysis is significantly faster than in an actual system (approximately 20 s). However, the computational cost for an analysis with a deployment time of 20 s would have required approximately 30 days. Additionally, because of the significant volume change during the deployment analysis, a remeshing scheme is implemented [38]. When the mesh is deemed poor during slat deployment, the FSI analysis is paused, and the slat/SCF mesh is rebuilt. Fluid flow and structural results are then mapped as initial conditions onto the continuation of FSI analysis with the new mesh.

Figure 11 shows the velocity contours during deployment for the composite-t2 and monolithic SMA SCFs. Note that the composite-t4 and SMN-t structurally behave in a manner similar to the composite-t2 SCF (e.g., they fail to deploy in flow) and are thus not shown for brevity. For both the tailored and monolithic designs, the magnitude of velocity across the surface of the slat and main wing leading edges generally increases as the high-lift devices deploy. This is due to the increasing effective camber of the wing and the creation of suction peaks on the main wing leading edge.

For all designs, in the range of 80–90% deployment, a jet of high velocity is present in the small gap between the main wing and the SCF. Additionally, during much of the deployment, flow over the main wing leading edge is prevented, resulting in flow separation off the slat cusp that reconnects downstream on the lower surface of the main wing, similar to a drooped leading edge. This behavior is also similar to an alternative aeroacoustic noise-reduction system known as the slat-gap filler [31]. Similar phenomena were observed during FSI analyses of a model scale SCF [38]. As seen in Fig. 11, only the monolithic SMA SCF successfully redeploy.

To better understand the structural response of the SCF during the deployment analysis, the kinetic energy, strain energy, and displacement of the nodes from the previous load case (Fig. 10) are examined. Note that the displacement shown here is measured with respect to the retracted configuration. For the first 80% (1.6 s) of the deployment, the kinetic energy is near zero, and the displacement is dominated by the deployment (quasi-steady increase with no fluctuations), indicating that there is no significant oscillatory response. This response is attributed to the contact between the SCF and main wing. Additionally, as expected, because the SCF is not exposed to flow at the start of

the FSI analysis, there is no initial large oscillatory behavior due to the sudden imposition of flow. However, after 80% deployment, all SCF designs lose contact with the main wing, resulting in the generation of the previously mentioned jet of high velocity flow. Since motion of the SCF is no longer restrained by the contact with the main wing, the jet of high-speed flow induces a high-frequency vibration with significant oscillations in the SCF as indicated by increases in kinetic energy and fluctuations in displacement and strain energy. Note that this behavior is expected to occur regardless of deployment speed. For SCF designs that did not successfully redeploy, as the slat reaches full deployment (2 s), the jet of high velocity flow diminishes, allowing for the designs to stabilize in a stowed configuration as indicated by the decreasing oscillations with lower frequencies in both kinetic and strain energy. This stabilization in the stowed configuration is further demonstrated in Fig. 12d, which shows the fluctuation in displacement of the nodes from Fig. 10 once the slat is fully deployed. For the monolithic SMA design, redeployment is clearly visible as indicated by the sudden changes in kinetic energy, strain energy, and displacement. With the exception of final stages of deployment where some designs fail to redeploy, the kinetic and strain energy curves from the FSI deployment analyses match well with the curves from the structure-only deployment analyses of the tailoring process (see Figs. 8 and 9). This is not unexpected, given that for a majority of the analyses the structural response of the SCF is primarily influenced by the contact with main wing and slat.

Prompted by the stabilization of many SCF designs in an undeformed configuration, examination of the pressure distribution acting on the SCF at the end of the analysis reveals a distribution that is considerably different than the one obtained from CFD analysis of the undeformed, fully deployed SCF. As shown in Fig. 13, the tailored designs exhibit a significantly higher positive pressure on the aft portion of the SCF. This considerably different pressure distribution acting on the tailored designs, only available through FSI analysis, is not accounted for during the tailoring process (see Sec. IV.A). Based on the results shown in Figs. 9 and 12 (especially the monolithic SMA design which exhibited the highest strain energy and redeployed), the tailored designs, which satisfy displacement constraints when fully deployed, do not store sufficient strain energy during the retraction process to redeploy under the unexpectedly different dynamic pressure loadings encountered. Overall, not accounting for the aerodynamic loadings encountered during deployment in the tailoring process is deemed to be the cause of failed redeployment for the tailored designs. Recall that one of the desirable features for a SCF design is reduced strain energy stored at the end of retraction as that correlates with a decrease in actuator loading. While the reduction in strain energy is important for physical implementations of the SCF,

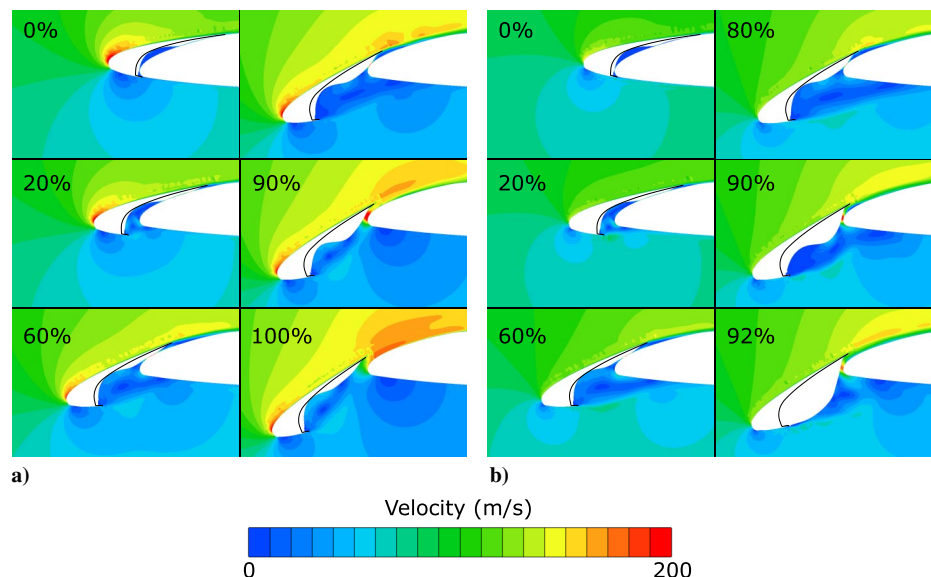


Fig. 11 Velocity contours during deployment for a) tailored composite-t2 design and b) monolithic SMA design under Mach 0.24 flow (deployment percentage indicated).

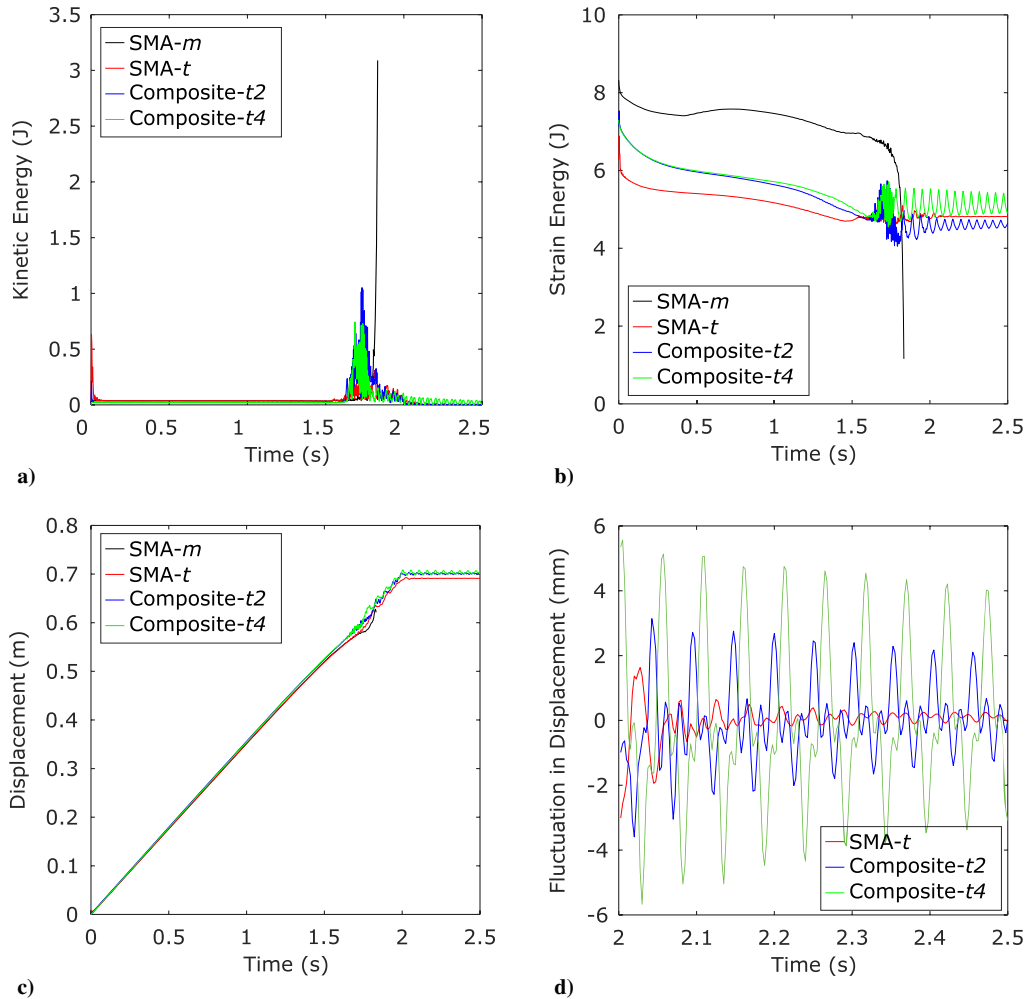


Fig. 12 Time histories of a) kinetic energy b) strain energy, c) displacement of node from Fig. 10 relative to retracted configuration, and d) fluctuation of displacement once the slat is fully deployed. Note that deployment occurs over 2 s. The SMA-m design is not shown in d as the FSI analysis ends upon SCF redeployment.

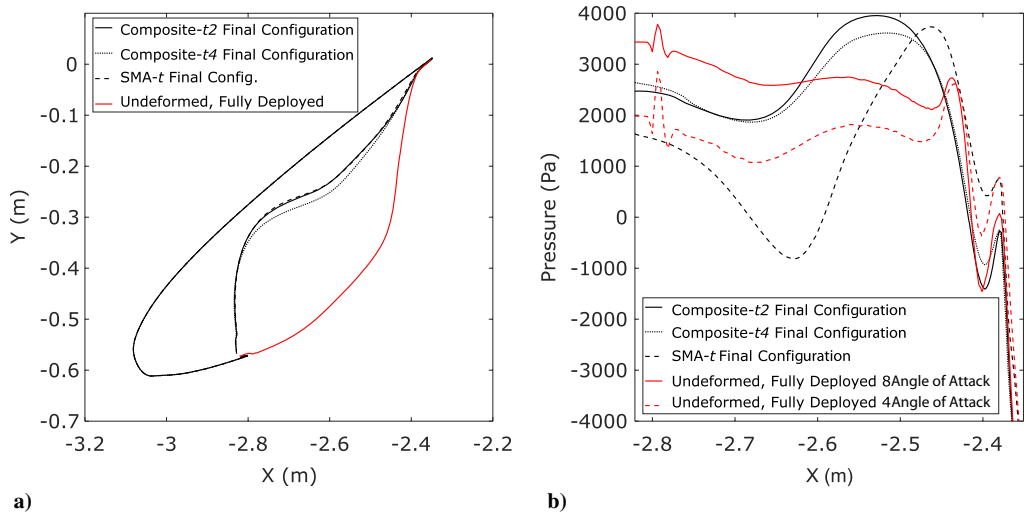


Fig. 13 Comparison between undeformed SCF and final configuration for tailored designs (i.e., unable to deploy) after FSI analysis of full deployment for a) shape and b) pressure distribution.

not including these unexpected aerodynamic loadings allowed the tailoring process to reduce the stored strain energy to levels that could not overcome the aerodynamic loading and redeploy the SCF. The inability to redeploy is also attributed to a reduced release of kinetic energy during snapback (see Figs. 8 and 9) compared to the

monolithic SMA SCF design. Recall that the tailoring process reduces the release of kinetic energy during retraction, resulting in two desirable design features: 1) prevention of violent collisions with the slat during retraction/stowage and 2) promotion of smoother retractions/redeployments. However, as previously discussed in

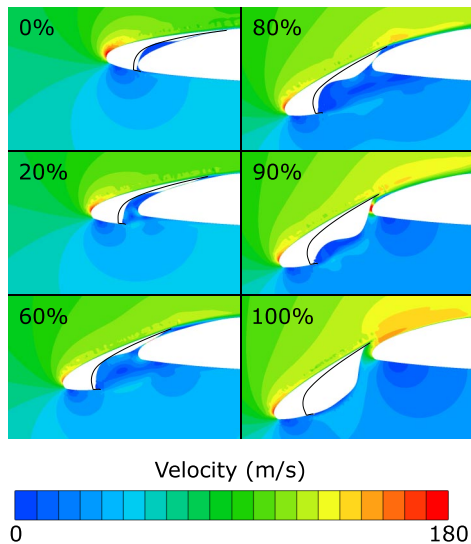


Fig. 14 Velocity contour plot during deployment for tailored composite-t4.

Sec. IV.A, a large release of kinetic energy also aids in redeployment of the SCF. It is suspected the tailoring process would result in an SCF design (composite or SMA) that is able to meet displacement constraints and fully redeploy under dynamic flow through the following improvements: 1) include FSI analysis or some alternate but likewise accurate representative pressure field during redeployment, 2) require more release of kinetic energy during deployment, or 3) limit the reduction of strain energy.

Based on the FSI results of the tailored designs assessed at Mach 0.24 and the results of the structural analyses from Sec. IV.B, the composite-t4 design is believed to be the most likely to redeploy under more conventional flow conditions because it exhibits the highest stored strain energy and peak reaction force during snapback (an indicator for potential redeployment) of the tailored designs, both of which may allow the SCF to overcome the aerodynamic loading. It is thus further tested in Mach 0.20 flow, the nominal landing speed. As shown in Fig. 14, under this standard flow condition, this design is able to redeploy, demonstrating that the tailoring process can result in viable SCF designs.

V. Conclusions

This Paper has investigated the design of the slat-cove filler, a morphing device that autonomously deploys into the cove between the leading-edge slat and wing of a transport aircraft for airframe noise reduction. The retraction and deployment of the SCF is governed by contact and loss of contact with the main wing as the leading-edge slat moves relative to the main wing.

Because of the nonlinearity of the problem, developing a robust design methodology is a challenge. The authors proposed and tested a design methodology that relies on a combination of structural analyses and CFD simulations. In particular, the influence of materials selection (shape-memory alloy and fiberglass composite) and the tailoring of the nonlinear SCF structural behavior are investigated via finite element analysis. The results of the structural analysis showed that stiffness-tailored SMA and composite designs were able to autonomously deploy from their retracted positions in the slat cove once contact with the main wing was lost. In fact, through varying the thickness and/or composite stacking sequence along the SCF arc length, it was possible to control the shape of the snap-through equilibrium curves to modify the amount of kinetic energy released during snaps and to reduce the required strain energy for stowage. Compared to a baseline monolithic (untailored) SMA SCF design [37,38], the kinetic energy released during snap-through of a composite SCF can be reduced by as much as -28.3% (composite-t3 design). Additionally, by modifying the equilibrium manifolds, a variety of behaviors including desirable design

features for both retraction (low stored SE, low release of KE during snap-through) and redeployment (high release of kinetic energy and peak force at snapback) could be obtained. These results suggested that, for portions of the span of a full wing SCF where strains are sufficiently low, the superelastic SMA material can be replaced with a tailored laminated composite design as the superelastic material behavior of the SCF is replicated by geometrically nonlinear behavior.

The behaviors of the monolithic SMA SCF, tailored composite SCFs, and tailored SMA SCF in a relevant flow environment were also investigated using FSI analysis to assess the viability of designs obtained via the tailoring process. An FSI model of the SCF was created, and computations were performed for two load cases: 1) high-lift devices in a fixed, fully deployed configuration and 2) high-lift device transient deployment. With the exception of the composite-t4 design, the SCF designs exhibited oscillatory behavior that decayed in time toward a constant value. However, comparison of deformation of the SCF under static loading from FSI (coupled) and CFD (uncoupled) analysis showed aeroelastic interactions between the SCF and the surrounding fluid that could destabilize the structure at higher flow velocities. Throughout most of the high-lift device deployment, the structural response of the SCF in flow (FSI analysis) and out of flow (structural analysis during the tailoring process) are relatively the same. However, only the monolithic SMA SCF and composite-t4 SCF successfully redeployed. Failure of the others to do so was attributed to the fact that the tailoring design process that created them did not account for the aerodynamic loading acting on the SCF during deployment, which was found to be considerably different than the loading when the SCF is fully deployed, nor the coupling between SCF deflection and the aerodynamic load distribution. Not including these loading effects allowed the tailoring process to reduce certain responses such as the stored strain energy (desirable for decreased actuator loads) below a critical level, resulting in the creation of designs that could not overcome the loadings encountered during deployment.

Future work will focus on refining the tailoring process and obtaining improved designs by incorporating FSI analyses of the deployment of the SCF during high-lift device articulation. Additionally, the effect of changing the peak kinetic energy experienced during slat articulation also needs to be investigated. A physical benchtop model of a composite design will also be built and tested to validate the computational tools discussed herein.

Appendix: Stress Analysis

Section III.D describes the constraints that must be accounted for during the design of a composite slat-cove filler. These include the Tsai-Wu failure criterion and transverse shear stresses of the composite solutions. Figure A1 shows the strains in the x direction for some of the studied SCF solutions as a function of simulation time. Maximum strains are identified at the snap-through. For each design, ϵ_x , the Tsai-Wu index, and σ_{xz} for each element of the SCF part are evaluated vs simulation time, thereby identifying the element and time step at which the component experiences the highest stresses and strains. The strains, TWFC, and σ_{xz} are then evaluated through the thickness of the identified element.

Figures A2a and A2a compare ϵ_x and σ_x through the thickness for the highest-strained element of the SMA-m, SMA-t, composite-t3, and composite-t4 SCF solutions. While the strains between composite and SMA SCFs are comparable, due to its intrinsic material properties, the SMAs show lower internal stresses through the thickness. Figure A2c shows the Twai-Wu failure index through the thickness of different composite designs. Note, for clarity, only the composite-m and composite-t4 designs are shown. As seen in the figure, both designs have the highest failure index in proximity to the bottom 30 deg orientation ply. Additionally, all designs satisfy the failure criterion of magnitude smaller than unity. Finally, in Fig. A2d, the transverse shear stress is plotted. Here, maximum values vary from -6.25 to 3.49 MPa. The interlaminar failure strength of the fiberglass reinforced plastic is estimated to be around 150 MPa in compression and 65.5 MPa in tension [52,53]. Hence, delamination damage due to elevated interlaminar stresses is unlikely.

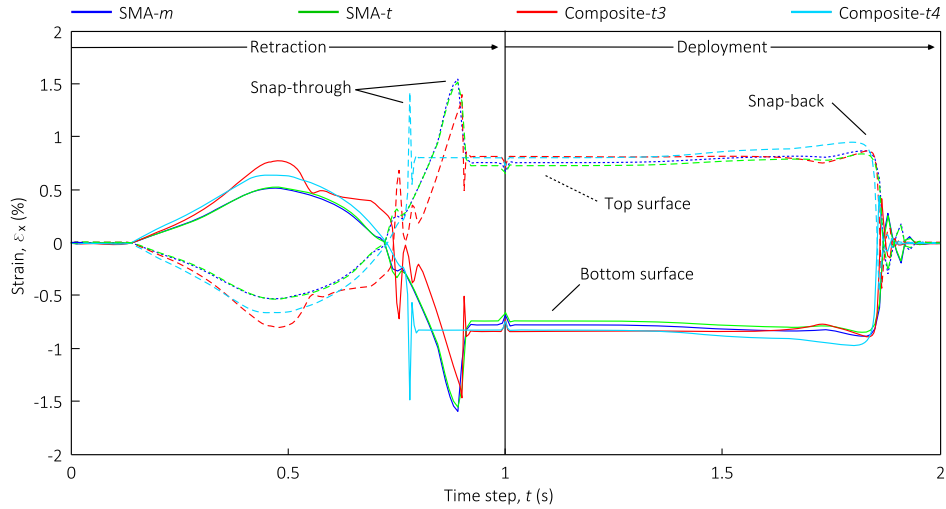


Fig. A1 Strains of the highest-strained elements during the simulation. In all cases, peaks in deformation are reached at snap-through of the SCF.

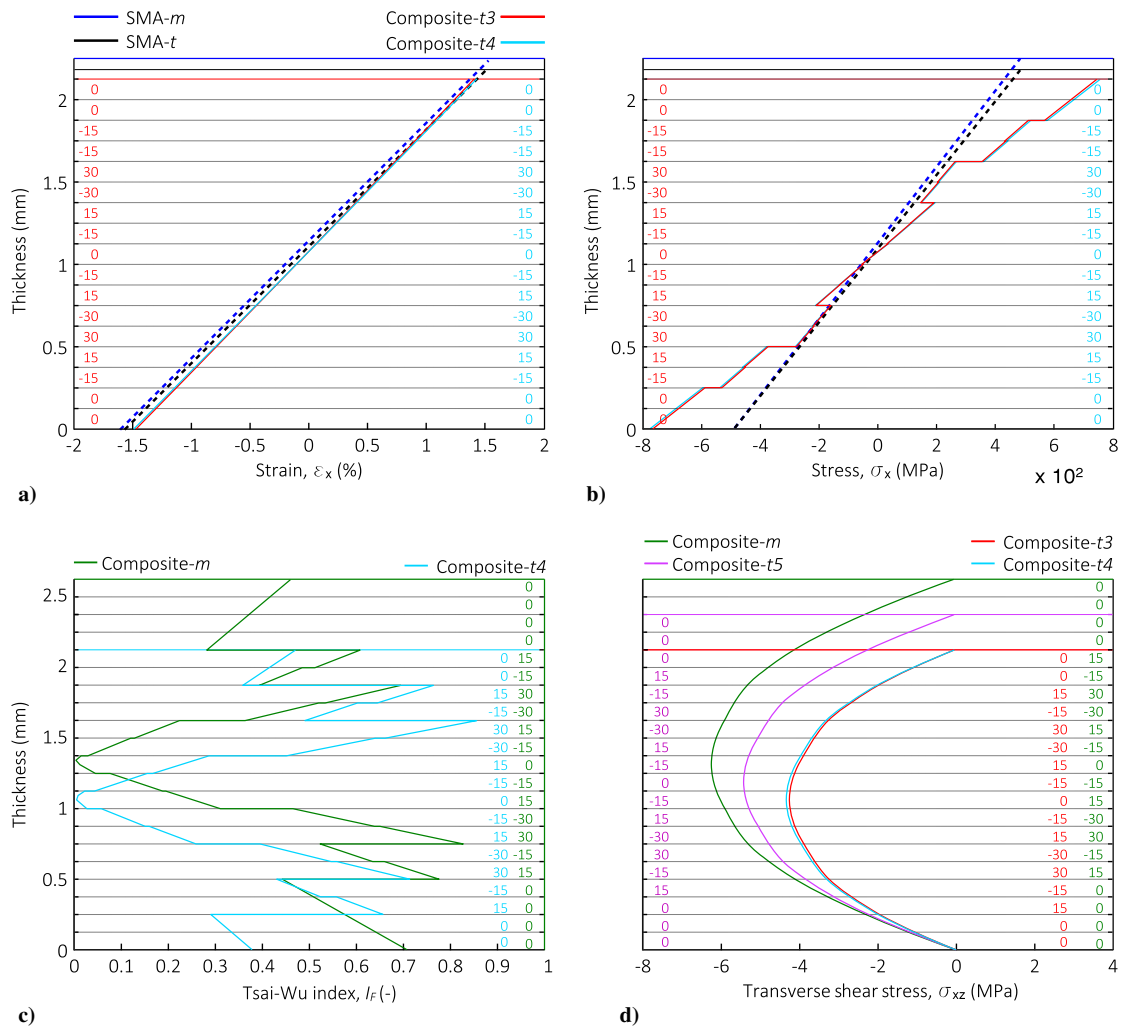


Fig. A2 Failure analysis of composite SCF: a) maximum strain ϵ_x and b) stress σ_x through the thickness of composite-t3 and composite-t4 compared to monolithic and tailored SMA SCFs, and c) the Tsai–Wu failure criterion and d) transverse shear stress σ_{xz} of different composite SCFs are compared.

Acknowledgments

G. Arena acknowledges support from the Engineering and Physical Sciences Research Council (EPSRC) through the support of the Doctoral Prize Fellowship (grant number EP/R513179/1). A. Pirrera acknowledges support from the EPSRC through an Early-Career Fellowship (grant number EP/M013170/1). R. Groh acknowledges the support of the Royal

Academy of Engineering through the research fellowship program (grant number RF/201718/17178). W. Scholten and D. Hartl acknowledge the support from NASA Langley Research Center, Structural Acoustics Branch (grant number NNL09AA00AA). Computational structural analysis was performed with a SIMULIA Abaqus research license. Computational fluid analysis was performed with a Cradle SC/Tetra license.

References

- [1] Wagg, D., Bond, I., Weaver, P., and Friswell, M., *Adaptive Structures: Engineering Applications*, Wiley, Hoboken, NJ, 2008, Chaps. 4–6.
- [2] Campanile, L. F., “Initial Thoughts on Weight Penalty Effects in Shape-Adaptable Systems,” *Journal of Intelligent Material Systems and Structures*, Vol. 16, No. 1, 2005, pp. 47–56. <https://doi.org/10.1177/1045389X05046692>
- [3] Sanders, B., Cowan, D., and Scherer, L., “Aerodynamic Performance of the Smart Wing Control Effectors,” *Journal of Intelligent Material Systems and Structures*, Vol. 15, No. 4, 2004, pp. 293–303. <https://doi.org/10.1177/1045389X04042799>
- [4] Weisshaar, T. A., “Morphing Aircraft Systems: Historical Perspectives and Future Challenges,” *Journal of Aircraft*, Vol. 50, No. 2, 2013, pp. 337–353. <https://doi.org/10.2514/1.C031456>
- [5] Williams, K., Chiu, G., and Bernhard, R., “Adaptive-Passive Absorbers Using Shape-Memory Alloys,” *Journal of Sound and Vibration*, Vol. 249, No. 5, 2002, pp. 835–848. <https://doi.org/10.1006/jsvi.2000.3496>
- [6] Scholten, W., Hartl, D., Strganac, T., and Turner, T., “Reduction of Actuation Loads in a Self-Deploying SMA-Based Slat-Cove Filler for a Transport Aircraft,” *Smart Materials, Adaptive Structures and Intelligent Systems*, Vol. 57304, American Soc. of Mechanical Engineers, Fairfield, NJ, 2015, p. V002T04A016.
- [7] Arrieta, A. F., Kuder, I. K., Rist, M., Waerber, T., and Ermanni, P., “Passive Load Alleviation Aerofoil Concept with Variable Stiffness Multi-Stable Composites,” *Composite Structures*, Vol. 116, Sept. 2014, pp. 235–242. <https://doi.org/10.1016/j.compstruct.2014.05.016>
- [8] Brinkmeyer, A., Pirrera, A., Santer, M., and Weaver, P. M., “Pseudo-Bistable Pre-Stressed Morphing Composite Panels,” *International Journal of Solids and Structures*, Vol. 50, Nos. 7–8, 2013, pp. 1033–1043. <https://doi.org/10.1016/j.ijsolstr.2012.11.019>
- [9] Eckstein, E., Pirrera, A., and Weaver, P. M., “Multi-Mode Morphing Using Initially Curved Composite Plates,” *Composite Structures*, Vol. 109, March 2014, pp. 240–245. <https://doi.org/10.1016/j.compstruct.2013.11.005>
- [10] Arena, G., Groh, R. M., Brinkmeyer, A., Theunissen, R., Weaver, P. M., and Pirrera, A., “Adaptive Compliant Structures for Flow Regulation,” *Proceedings of the Royal Society*, Vol. 473, No. 2204, 2017, p. 20170334. <https://doi.org/10.1098/rspa.2017.0334>
- [11] Gomez, M., Moulton, D. E., and Vella, D., “Critical Slowing Down in Purely Elastic ‘Snap-Through’ Instabilities,” *Nature Physics*, Vol. 13, No. 2, 2017, p. 142–145. <https://doi.org/10.1038/nphys3915>
- [12] Daynes, S., Weaver, P. M., and Trevarthen, J., “A Morphing Composite Air Inlet with Multiple Stable Shapes,” *Journal of Intelligent Material Systems and Structures*, Vol. 22, No. 9, 2011, pp. 961–973. <https://doi.org/10.1038/nphys3915>
- [13] Runkel, F., Reber, A., Molinari, G., Arrieta, A. F., and Ermanni, P., “Passive Twisting of Composite Beam Structures by Elastic Instabilities,” *Composite Structures*, Vol. 147, July 2016, pp. 274–285. <https://doi.org/10.1016/j.compstruct.2016.02.080>
- [14] Arena, G., Groh, R. M. J., Theunissen, R., Weaver, P., and Pirrera, A., “Design and Testing of a Passively Adaptive Inlet,” *Smart Materials and Structures*, Vol. 27, No. 8, 2018, Paper 085019. <https://doi.org/10.1088/1361-665X/aacf>
- [15] Danso, L. A., and Karpov, E. G., “Cusp Singularity-Based Bistability Criterion for Geometrically Nonlinear Structures,” *Extreme Mechanics Letters*, Vol. 13, May 2017, pp. 135–140. <https://doi.org/10.1016/j.eml.2017.01.001>
- [16] Groh, R. M. J., Avitabile, D., and Pirrera, A., “Generalised Path-Following for Well-Behaved Nonlinear Structures,” *Computer Methods in Applied Mechanics and Engineering*, Vol. 331, April 2018, pp. 394–426. <https://doi.org/10.1016/j.cma.2017.12.001>
- [17] Gleine, W., Mau, K., and Carl, U., U.S. Patent Application for “Aerodynamic Noise Reducing Structure for Aircraft Wing Slats,” Docket No. 6,394,396, filed 28 May 2002.
- [18] Khorrami, M. R., Berkman, M. E., and Choudhari, M., “Unsteady Flow Computations of a Slat with a Blunt Trailing Edge,” *AIAA Journal*, Vol. 38, No. 11, 2000, pp. 2050–2058. <https://doi.org/10.2514/2.892>
- [19] Singer, B. A., Lockard, D. P., and Brentner, K. S., “Computational Aeroacoustic Analysis of Slat Trailing-Edge Flow,” *AIAA Journal*, Vol. 38, No. 9, 2000, pp. 1558–1564. <https://doi.org/10.2514/2.1177>
- [20] Streett, C., Casper, J., Lockard, D., Khorrami, M., Stoker, R., Elkoby, R., Wenneman, W., Underbrink, J., Wenneman, W., and Underbrink, J., “Aerodynamic Noise Reduction for High-Lift Devices on a Swept Wing Model,” *44th AIAA Aerospace Sciences Meeting and Exhibit*, AIAA Paper 2006-0212, 2006. <https://doi.org/10.2514/6.2006-212>
- [21] Home, W., James, K., Arledge, T., Soderman, P., Burnside, N., and Jaeger, S., “Measurements of 26%-Scale 777 Airframe Noise in the NASA AMES 40-by 80 Foot Wind Tunnel,” *11th AIAA/CEAS Aeroacoustics Conference*, AIAA Paper 2005-2810, 2005. <https://doi.org/10.2514/6.2005-2810>
- [22] Zhang, Y., O’Neill, A., Cattafesta, L. N., Pascioni, K., Choudhari, M., Khorrami, M. R., Lockard, D. P., and Turner, T., “Assessment of Noise Reduction Concepts for Leading-Edge Slat Noise,” *2018 AIAA/CEAS Aeroacoustics Conference*, AIAA Paper 2018-3461, 2018. <https://doi.org/10.2514/6.2018-3461>
- [23] Reis, D. C., Coelho, E. L., Lima Pereira, L. T., Catalano, F., and Lima, L., “A Study on the 3D Effects of Slat Cove Fillers,” *25th AIAA/CEAS Aeroacoustics Conference*, AIAA Paper 2019-2406, 2019. <https://doi.org/10.2514/6.2019-2406>
- [24] Leaton, A., Scholten, W., Lieb, K., Hartl, D. J., Strganac, T., and Turner, T. L., “Aerostructural and Aeroacoustic Experimental Testing of Shape Memory Alloy Slat Cove Filler,” *AIAA SciTech 2020 Forum*, AIAA Paper 2020-1040, 2020. <https://doi.org/10.2514/6.2020-1040>
- [25] Imamura, T., Ura, H., Yokokawa, Y., Enomoto, S., Yamamoto, K., and Hirai, T., “Designing of Slat Cove Filler as a Noise Reduction Device for Leading-Edge Slat,” *13th AIAA/CEAS Aeroacoustics Conference (28th AIAA Aeroacoustics Conference)*, AIAA Paper 2007-3473, 2007. <https://doi.org/10.2514/6.2007-3473>
- [26] Tao, J., and Sun, G., “A Novel Optimization Method for Maintaining Aerodynamic Performances in Noise Reduction Design,” *Aerospace Science and Technology*, Vol. 43, June 2015, pp. 415–422. <https://doi.org/10.1016/j.ast.2015.04.008>
- [27] Khorrami, M., and Lockard, D., “Effects of Geometric Details on Slat Noise Generation and Propagation,” *12th AIAA/CEAS Aeroacoustics Conference (27th AIAA Aeroacoustics Conference)*, AIAA Paper 2006-2664, 2006. <https://doi.org/10.2514/6.2006-2664>
- [28] Mau, K., and Dobrzynski, W., U.S. Patent Application for “Flexible Airflow Separator to Reduce Aerodynamic Noise Generated by a Leading Edge Slat on an Aircraft Wing,” Docket No. 6,789,769, filed 14 Sept. 2004.
- [29] Ortmann, J., and Wild, J., “Effect of Acoustic Slat Modifications on Aerodynamic Properties of High-Lift Systems,” *Journal of Aircraft*, Vol. 44, No. 4, 2007, pp. 1258–1263. <https://doi.org/10.2514/1.26307>
- [30] Huang, H., Li, W., and Wang, F., “Slat Noise Suppression with Mass Injection,” *Journal of Aircraft*, Vol. 52, No. 1, 2015, pp. 31–41. <https://doi.org/10.2514/1.C032364>
- [31] Turner, F., and Long, D., “Development of a SMA-Based, Slat-Gap Filler for Airframe Noise Reduction,” *23rd AIAA/AHS Adaptive Structures Conference*, AIAA Paper 2015-0730, 2015. <https://doi.org/10.2514/6.2015-0730>
- [32] Zhang, Y., Cattafesta, L. N., Pascioni, K. A., Choudhari, M. M., Lockard, D. P., Khorrami, M. R., and Turner, T., “Slat Noise Control Using a Slat Gap Filler,” *AIAA Aviation 2020 Forum*, AIAA Paper 2020-2553, 2020. <https://doi.org/10.2514/6.2020-2553>
- [33] Scholten, W. D., Hartl, D. J., Turner, T. L., and Kidd, R. T., “Development and Analysis-Driven Optimization of Superelastic Slat-Cove Fillers for Airframe Noise Reduction,” *AIAA Journal*, Vol. 54, No. 3, 2015, pp. 1078–1094. <https://doi.org/10.2514/1.J054011>
- [34] Turner, T., Kidd, R., Hartl, D., and Scholten, W., “Development of a SMA-Based, Slat-Cove Filler For Reduction of Aeroacoustic Noise Associated with Transport-Class Aircraft Wings,” *Smart Materials, Adaptive Structures and Intelligent Systems*, Vol. 56048, American Soc. of Mechanical Engineers, Fairfield, NJ, 2013, p. V002T02A005.
- [35] Lagoudas, D. C., *Shape Memory Alloys: Modeling and Engineering Applications*, Springer-Verlag, New York, 2008, Chaps. 1–4.
- [36] Scholten, W., Patterson, R., Hartl, D., Strganac, T., Volpi, J., Chapelon, Q., and Turner, T., “Noise Reduction in a High Lift Wing Using SMAs: Computational Fluid-Structural Analysis,” *ASME 2016 Conference on Smart Materials, Adaptive Structures and Intelligent Systems*, American Soc. of Mechanical Engineers, Fairfield, NJ, 2016, p. V001T02A009. <https://doi.org/10.1115/SMASIS2016-9196>

- [37] Scholten, W., Patterson, R., Hartl, D., Strganac, T., Chapelon, Q., and Turner, T., "Computational and Experimental Fluid-Structure Interaction Assessment of a High-Lift Wing with a Slat-Cove Filler for Noise Reduction," *AIAA SciTech 2017 Forum*, AIAA Paper 2017-0732, 2017.
- [38] Scholten, W., Patterson, R., Eustice, M., Cook, S., Hartl, D., Strganac, T., and Turner, T., "Aerodynamic and Structural Evaluation of an SMA Slat-Cove Filler Using Computational and Experimental Tools at Model Scale," *Smart Materials, Adaptive Structures and Intelligent Systems*, Vol. 51944, American Soc. of Mechanical Engineers, Fairfield, NJ, 2018, p. V001T04A019.
- [39] Patterson, R., Scholten, W., Strganac, T., Turner, T., and Hartl, D., "Experimental Validation of a Shape-Memory Alloy Slat-Cove Filler: Structural Response and Computational Model Development," *Journal of Intelligent Material Systems and Structures*, Vol. 31, No. 17, 2020, pp. 1986–2001.
<https://doi.org/10.1177/1045389X20942321>
- [40] Turner, T. L., Moore, J., and Long, D. L., "Computational Modeling of a Mechanized Bench-Top Apparatus for Leading-Edge Slat Noise Treatment Device Prototypes," *25th AIAA/AHS Adaptive Structures Conference*, AIAA Paper 2017-1874, 2017.
<https://doi.org/10.2514/6.2017-1874>
- [41] Vassberg, J. C., DeHaan, M. A., Rivers, M. S., and Wahls, R. A., "Retrospective on the Common Research Model for Computational Fluid Dynamics Validation Studies," *Journal of Aircraft*, Vol. 55, No. 4, 2018, pp. 1325–1337.
<https://doi.org/10.2514/1.C034906>
- [42] Lacy, D. S., and Sclafani, A. J., "Development of the High Lift Common Research Model (hl-crm): A Representative High Lift Configuration for Transonic Transports," *54th AIAA Aerospace Sciences Meeting*, AIAA Paper 2016-0308, 2016.
<https://doi.org/10.2514/6.2016-030>
- [43] *Abaqus Documentation*, 6th ed., Dassault Systèmes (SIMULIA), Paris, France, 2016.
- [44] Langelaar, M., and van Keulen, F., "Modeling of Shape Memory Alloy Shells for Design Optimization," *Computers & Structures*, Vol. 86, No. 9, 2008, pp. 955–963.
<https://doi.org/10.1016/j.compstruc.2007.04.017>
- [45] Auricchio, F., and Sacco, E., "A One-Dimensional Model for Super-elastic Shape-Memory Alloys with Different Elastic Properties Between Austenite and Martensite," *International Journal of Non-Linear Mechanics*, Vol. 32, No. 6, 1997, pp. 1101–1114.
[https://doi.org/10.1016/S0020-7462\(96\)00130-8](https://doi.org/10.1016/S0020-7462(96)00130-8)
- [46] *SC/Tetra User's Guide*, Software Cradle, Osaka, Japan, 2015.
- [47] Menter, F., "Zonal Two Equation $k - \omega$ Turbulence Models for Aerodynamic Flows," AIAA Paper 1993-2906, 1993.
<https://doi.org/10.2514/6.1993-2906>
- [48] Arena, G., Scholten, W., Groh, R., Pirrera, D., Hartl, A., and Turner, T., "A Tailored Nonlinear Stat-Cove Filler for Airframe Noise Reduction," *Proceedings of the ASME 2018 Conference on Smart Materials, Adaptive Structures and Intelligent Systems*, American Soc. of Mechanical Engineers Paper SMASIS2018-8079, Fairfield, NJ, 2018, p. V001T03A017.
<https://doi.org/10.1115/SMASIS2018-8079>
- [49] Tsai, S. W., and Wu, E. M., "A General Theory of Strength for Anisotropic Materials," *Journal of Composite Materials*, Vol. 5, No. 1, 1971, pp. 58–80.
<https://doi.org/10.1177/002199837100500106>
- [50] Cui, W., Wisnom, M., and Jones, M., "A Comparison of Failure Criteria to Predict Delamination of Unidirectional Glass/Epoxy Specimens Waisted Through the Thickness," *Composites*, Vol. 23, No. 3, 1992, pp. 158–166.
[https://doi.org/10.1016/0010-4361\(92\)90436-X](https://doi.org/10.1016/0010-4361(92)90436-X)
- [51] Patni, M., Minera, S., Groh, R., Pirrera, A., and Weaver, P., "Three-Dimensional Stress Analysis for Laminated Composite and Sandwich Structures," *Composites Part B: Engineering*, Vol. 155, Dec. 2018, pp. 299–328.
<https://doi.org/10.1016/j.compositesb.2018.08.127>
- [52] Bibo, G., Hogg, P., and Kemp, M., "Mechanical Characterisation of Glass-and Carbon-Fibre-Reinforced Composites Made with Non-Crimp Fabrics," *Composites Science and Technology*, Vol. 57, Nos. 9–10, 1997, pp. 1221–1241.
[https://doi.org/10.1016/S0266-3538\(97\)00053-5](https://doi.org/10.1016/S0266-3538(97)00053-5)
- [53] Soden, P., Hinton, M., and Kaddour, A., "Lamina Properties, Lay-Up Configurations and Loading Conditions for a Range of Fibre Reinforced Composite Laminates," *Failure Criteria in Fibre-Reinforced-Polymer Composites*, Elsevier, New York, 2004, pp. 30–51.